CHEMICAL REVIEWS

REVIEW

pubs.acs.org/CR

# Plasmonic Nanoantennas: Fundamentals and Their Use in Controlling the Radiative Properties of Nanoemitters

Vincenzo Giannini,* Antonio I. Fernández-Domínguez, Susannah C. Heck, and Stefan A. Maier

Department of Physics, Imperial College London, London SW7 2AZ, United Kingdom

## CONTENTS

1. Introduction 3888
2. Scattering of Light by Metal Nanoparticles 3889
   2.1. Nanoparticle Cross Section and Optical Theorem 3889
   2.2. Optical Properties of Metals 3890
   2.3. Localized Surface Plasmon Resonances 3891
   2.4. Optical Nanoantennas 3892
   2.5. Dark Modes and Fano Resonances 3894
   2.6. Nanoparticle Arrays 3896
3. Fabrication and Characterization 3897
4. Emitters Close to Metal Nanoparticles: Interaction with Localized Surface Plasmons 3899
   4.1. Spontaneous Emission Engineering: Purcell Effect 3900
   4.2. Weak Coupling 3900
   4.3. Strong Coupling 3902
5. Nanoparticle Applications 3902
   5.1. Surface-Enhanced Fluorescence 3902
   5.2. Surface-Enhanced Raman Scattering 3904
   5.3. Plasmonic Solar Cells 3904
   5.4. Nanomedicine 3906
6. Conclusions 3907
Author Information 3907
Biographies 3907
Acknowledgment 3908
References 3908
Note Added after ASAP Publication 3912

## 1. INTRODUCTION

When light interacts with a metal nanoparticle (NP), its conduction electrons can be driven by the incident electric field in collective oscillations known as *localized surface plasmon resonances* (LSPRs). These give rise to a drastic alteration of the incident radiation pattern and to striking effects such as the subwavelength localization of electromagnetic (EM) energy, the formation of high intensity hot spots at the NP surface, or the directional scattering of light out of the structure. LSPRs can also couple to the EM fields emitted by molecules, atoms, or quantum dots placed in the vicinity of the NP, leading in turn to a strong modification of the radiative and nonradiative properties of the emitter. Since LSPRs enable an efficient transfer of EM energy from the near to the far-field of metal NPs and *vice versa*, we can consider plasmonic nanostructures as *nanoantennas*, because they operate in a similar way to radio antennas but at higher frequencies. Typically, plasmonic nanoantennas at optical frequencies are made of gold and silver due to their good metallic properties and low absorption.

Controlling and guiding light has been one of science's most influential achievements. It affects everyday life in many ways, such as the development of telescopes, microscopes, spectrometers, and optical fibers, to name but a few. These examples exploit the wave nature of light and are based on the reflection, refraction and diffraction of light by optical elements such as mirrors, lenses or gratings. However, the wave nature of light limits the resolution to which an object can be imaged, as well as the size of the transverse cross section of efficient guiding structures to the wavelength dimension. Plasmonic resonances in nanoantennas overcome these constraints, allowing unprecedented control of light−matter interactions within subwavelength volumes (i.e., within the nanoscale at optical frequencies). Such properties have attracted much interest lately, due to the implications they have both in fundamental research and in technological applications.[1−8]

Metal NPs have been used since antiquity. Due to their strong scattering properties in the visible range, they show attractive colors. One of their first applications, dating back to the Roman Empire more than 2000 years ago, was as a colorant for clothing. In art, they were used to stain window glass and ceramics. Obviously, it was not known then that the colorants being used contained metal NPs or that the spectacular colors were due to the excitation of LSPRs. The first reported intentional production of metal NPs dates from 1857, when Faraday synthesized gold colloids.[9] However, at the time there was not much interest in understanding the physics behind the optical properties of colloids due to the impossibility of synthesizing NPs with well-controlled shapes and sizes, as well as the lack of accurate detection techniques.

The first theoretical work on the scattering of light by particles smaller than the incident wavelength was carried out by Lord Rayleigh at the end of the 19th century.[10,11] He analyzed the diffusion of light by diluted gases, and his theory explained physical phenomena such as the blueness of the sky, the redness of the sunset, or the yellow color of the sun. Mie took the next step forward by deriving an analytical solution to Maxwell's equations to describe the interaction of light with spheres of arbitrary radius and composition.[12] Subsequently, based on the results of Rayleigh and Mie, Gans considered elliptical geometries. He demonstrated that the optical response of metal NPs is

**Special Issue:** 2011 Plasmonics

**Received:** August 17, 2010
**Published:** March 24, 2011





dx.doi.org/10.1021/cr1002672 | *Chem. Rev.* 2011, 111, 3888–3912

strongly shape dependent[13] and explained the origin of the different colors produced when white light is incident on colloidal solutions of elliptically shaped nanoparticles with different aspect ratios.

After Gans' work, the discovery of the surface-enhanced Raman scattering (SERS) effect in 1974[14−16] renewed interest in metal NPs due to the possibility of enhancing the Raman emission of molecules adsorbed onto a metal surface. A large number of publications on the physics taking place when molecules are in close proximity to metal structures followed. Eventually, this research has led to the development of nanoplasmonics, a multidisciplinary field devoted to the exploration of the unprecedented control of light and light−matter interactions that the strong localized EM fields associated with plasmonic resonances provide.

Concentrating light into small volumes leads to fascinating phenomena. LSPRs supported by pairs of nanoantennas with a small gap between them or by nanoantennas with particular shapes, such as nanostars,[17,18] are able to greatly amplify local EM fields, making these structures ideal for use in surface-enhanced fluorescence[19−29] (SEF) and SERS.[18,30−42] The small mode volume of LSPRs also increases the photonic local density of states (LDOS)[43,44] close to the NP, enabling the modification of the optical properties (decay rate and quantum efficiency) of emitters placed in its vicinity. Controlling local field enhancements and modifying of the LDOS in plasmonic nanoantennas has made single-molecule detection possible.[28,45,46] Nanoantennas are also extremely suitable for biological applications because they enable the tracking of emission from markers in cells with subdiffraction limit resolution, as well as the destruction of cancer cells using the resistive heating of resonant NPs.[33,39,47−55]

In this review, we describe the main theoretical concepts behind the interaction of light with nanoantennas and the emitter decay rate modification due to plasmonic cavity effects. We provide a brief overview of the fabrication and characterization methods available and discuss some nanoantenna applications, such as SEF, SERS, photovoltaics, and nanomedicine. The article is organized as follows: In section 2, we introduce the excitation of LSPRs in metal NPs and present concepts such as dark modes and Fano resonances. Section 3 includes a brief overview of fabrication and characterization techniques available in nanoplasmonics. In section 4, we show that LSPRs can influence the radiative and nonradiative properties of nanoemitters and show how nanoantennas can be used to control their optical properties. Finally, we outline some promising applications of plasmonic nanoantennas in section 5, such as nanomedicine and plasmonic solar cells.

## 2. SCATTERING OF LIGHT BY METAL NANOPARTICLES

### 2.1. Nanoparticle Cross Section and Optical Theorem

Figure 1 shows the general problem considered in this section: the interaction of light with a particle of arbitrary geometry and dielectric properties.[56,57] Given the incident EM field and the shape, size, and relative dielectric function (or relative permittivity), $\varepsilon$, of the scatterer, the objective is to determine the electric, $\mathbf{E}$, and magnetic, $\mathbf{H}$, fields at all points in space. In both the scatterer and the embedding medium of lossless dielectric constant $\varepsilon_d$, the EM fields must satisfy the macroscopic Maxwell's equations. At the particle boundary, continuity conditions must be imposed on the different components of the fields.[58] In general, this is a complex problem that must be solved numerically, although analytical expressions can be obtained for

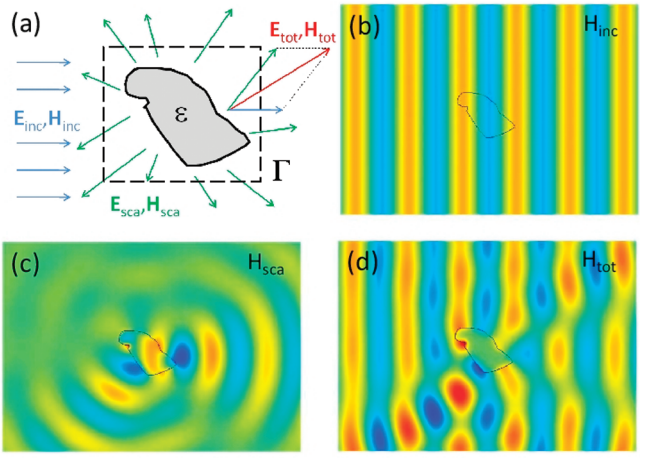


**Figure 1.** (a) Sketch of the scattering of p-polarized light by a metal particle with translational symmetry along the $z$-axis (out of the page), showing the decomposition of the EM fields into incident and scattered contributions. (b−d) Incident, scattered, and total magnetic field for the case of a metallic NP of permittivity $\varepsilon = -10 + i$. The color scale is the same for these three panels and ranges from $\mathbf{H}_z = -1$ (blue) to $\mathbf{H}_z = 1$ (red), in normalized units.

simple geometries or certain approximations.[59−61] Note that although all the expressions and definitions presented below have a general character, we will assume that the particle size is of the order or much smaller than the wavelength, $\lambda$, of the incoming field. In order to gain physical insight into the problem, it is convenient to write the total fields as a superposition of incident and scattered fields

$$\begin{aligned} \mathbf{E}_{tot} &= \mathbf{E}_{inc} + \mathbf{E}_{sca} \\ \mathbf{H}_{tot} &= \mathbf{H}_{inc} + \mathbf{H}_{sca} \end{aligned} \tag{1}$$

The incident field is the light illuminating the particle, while the scattered field accounts for the EM waves that are reirradiated by the particle when interacting with the incoming radiation (see panel a of Figure 1). We can express the conservation of energy for the problem as

$$\mathbf{S}_{tot} = \mathbf{S}_{inc} + \mathbf{S}_{sca} + \mathbf{S}_{ext} \tag{2}$$

where $\mathbf{S}_{inc} = {}^1/_2\mathrm{Re}\{\mathbf{E}_{inc} \times \mathbf{H}^*_{inc}\}$ and $\mathbf{S}_{sca} = {}^1/_2\mathrm{Re}\{\mathbf{E}_{sca} \times \mathbf{H}^*_{sca}\}$ are the time-averaged Poynting vectors (EM power flow) corresponding to the incoming and scattered waves. The term $\mathbf{S}_{tot} = {}^1/_2\mathrm{Re}\{\mathbf{E}_{tot} \times \mathbf{H}^*_{tot}\}$ denotes the total energy traveling in the system, while $\mathbf{S}_{ext} = {}^1/_2\mathrm{Re}\{\mathbf{E}_{inc} \times \mathbf{H}^*_{sca} + \mathbf{E}_{sca} \times \mathbf{H}^*_{inc}\}$ describes the EM power arising due to the interference of the incident and scattered fields.

By integrating eq 2 through any closed surface, $\Gamma$, containing the particle [see Figure 1a], we find a simple relation for the different energy channels present in the system. We can assume without loss of generality that the incoming light is a plane wave, having $\int_\Gamma \mathbf{S}_{inc}\, \mathbf{ds} = 0$. Thus, the energy scattered and absorbed by the particle are given by $W_{sca} = \int_\Gamma \mathbf{S}_{sca}\, \mathbf{ds}$ and $W_{abs} = -\int_\Gamma \mathbf{S}_{tot}\, \mathbf{ds}$, respectively. Notice that the link between the total field and the absorbed energy resides in the fact that the embedding medium is lossless, whereas $\mathrm{Im}\{\varepsilon\} > 0$ for the metallic particle. The minus sign indicates the inward orientation of the surface, which leads to $W_{abs} > 0$. The interference term gives the energy extinct in the scattering process, $W_{ext} = -\int_\Gamma \mathbf{S}_{ext}\, \mathbf{ds}$, whose physical meaning can be understood through the energy relation,


dx.doi.org/10.1021/cr1002672 |Chem. Rev. 2011, 111, 3888–3912

$W_{ext} = W_{abs} + W_{sca}$, which follows from eq 2. Thus, $W_{ext}$ corresponds to the total energy removed from the incident field by both scattering and absorption.

We introduce now the concept of an EM cross section. As we have seen, absorption and scattering remove energy from the incoming EM field when light interacts with particles. Thus, we can associate an effective cross section to each of these mechanisms,

$$\begin{aligned} \sigma_{abs} &= W_{abs}/|\mathbf{S}_{inc}| \\ \sigma_{sca} &= W_{sca}/|\mathbf{S}_{inc}| \end{aligned} \tag{3}$$

where $|\mathbf{S}_{inc}| = {}^1/_2 c\varepsilon_0(\varepsilon_d)^{1/2}|E_0|^2$ is the power flow per unit area carried by the incident linearly polarized plane wave, $\mathbf{E}_{inc} = E_0\, e^{i(\varepsilon_d)^{1/2}k_0\mathbf{r}\cdot\mathbf{n}_0}\,\mathbf{e}_0$. $\mathbf{n}_0$ and $\mathbf{e}_0$ are unit vectors along the direction of illumination and polarization, respectively, and $k_0 = \omega/c = 2\pi/\lambda$ is the modulus of the wavevector in vacuum. Energy conservation enables us to define the extinction cross section as

$$\sigma_{ext} = W_{ext}/|\mathbf{S}_{inc}| = \sigma_{abs} + \sigma_{sca} \tag{4}$$

$\sigma_{ext}$ is a measure of the total effective area that the EM fields perceive when interacting with the particle. An efficiency factor, $Q$, associated with each cross section is defined in the literature by normalizing the cross section, $\sigma$, to the physical cross-sectional area of the particle projected onto a plane perpendicular to the direction of illumination.

Panels b−d of Figure 1 show the incident, scattered, and total magnetic field components for the particle geometry shown in Figure 1a, illuminated from the left by a transverse magnetic plane wave (magnetic field points out of the plane). The permittivity considered in the calculation is $\varepsilon = -10 + i$, which corresponds to Au at $\lambda = 620$ nm.[62] For simplicity, translational symmetry has been imposed along the direction normal to the page. These panels illustrate the decomposition of the EM fields, which give rise to the various EM cross sections we have defined above.

We can get a deeper understanding of the phenomenon of light scattering by metal NPs by considering the expression for the scattered fields in the far-field ($r \gg \lambda$). It can be demonstrated[58] that, for any particle geometry and dielectric properties, the scattered electric field far from the particle has the form

$$\mathbf{E}_{sca} = E_0 \frac{e^{i\sqrt{\varepsilon_d}k_0 r}}{\sqrt{\varepsilon_d}k_0 r}\,\mathbf{f}(\mathbf{n}, \mathbf{n}_0) \tag{5}$$

where $\mathbf{f}(\mathbf{n},\mathbf{n}_0)$ gives the amplitude and polarization of the scattered electric field along the arbitrary direction $\mathbf{n}$. By introducing eq 5 and the expression for $\mathbf{H}_{sca}$ into $\mathbf{S}_{ext}$, we can write the extinction cross section as

$$\sigma_{ext} = \frac{4\pi}{\varepsilon_d {k_0}^2}\,\mathrm{Im}\{\mathbf{e}_0 \cdot \mathbf{f}(\mathbf{n}_0, \mathbf{n}_0)\} \tag{6}$$

This is a very powerful relation, which indicates that the total power removed from the incoming EM field by the particle only depends on the scattering amplitude along the forward direction, $\mathbf{f}(\mathbf{n}_0,\mathbf{n}_0)$. Note that this is a striking result, because extinction combines both absorption and scattering by the particle in all directions. Equation 6 is usually known as the *Optical Theorem*[63] and is valid not only in electromagnetism but also in acoustics and quantum mechanics.[64]

## 2.2. Optical Properties of Metals

The optical response of noble metals are described by a frequency-dependent complex dielectric function, $\varepsilon(\omega)$, which relates the value of electric, **E**, and displacement field, **D**, within them. Experimental measurements of the optical properties of a range of solids, including gold and silver, can be found in the literature.[62,65−69] Qualitatively, we can identify two different mechanisms that contribute to $\varepsilon(\omega)$ in metals:[59]

- The fast response of conduction electrons, which can move quasi-freely in the bulk material when experiencing an external EM excitation, yields a Drude−Sommerfeld contribution to $\varepsilon(\omega)$

$$\varepsilon_{Drude}(\omega) = \varepsilon_\infty - \frac{{\omega_p}^2}{\omega(\omega + i\gamma)} \tag{7}$$

  where $\omega_p$ (metal plasma frequency) corresponds to the eigenfrequency of the electronic oscillations, $\gamma$ (collision frequency) reflects the damping experienced by the electrons when moving within the material, and $\varepsilon_\infty$ accounts for the residual polarization due to the positive background of the ion cores.
- The electronic interband transitions occur when the energy of the incoming photon is large enough to overcome the band gap and promote valence (bound) electrons to the conduction band of the material. This effect can be taken into account in $\varepsilon(\omega)$ by means of a Lorentz-like term

$$\varepsilon_{Lorentz}(\omega) = \frac{\Delta\varepsilon {\Omega_p}^2}{{\Omega_p}^2 - \omega^2 - i\Gamma\omega} \tag{8}$$

  where, in analogy to the Drude formula (eq 7), $\Omega_p$ and $\Gamma$ are the plasma and damping frequencies for the bound electrons, and the parameter $\Delta\varepsilon$ weights the contribution of the given interband transition to the dielectric function. In general, several Lorentzian terms can be added to $\varepsilon(\omega)$ to describe the effect of different interband transitions and enable a better fit to experimental data. The integrated effect of high-energy electronic transitions also modifies $\varepsilon_\infty$ in eq 7, because it governs the metal response in the high-frequency limit.

In panels a and b of Figure 2, we plot the real and imaginary parts of the permittivity of gold in the visible and near-infrared parts of the EM spectrum. The dielectric function, calculated using data measured by Johnson and Christy,[62] is plotted as black dots, while the red and blue lines correspond to Drude and Drude−Lorentz fits to the experimental values. At long wavelengths ($\lambda \geq 600$ nm), $\varepsilon(\omega)$ is governed by its large negative real part. This is a consequence of the fast response of conduction electrons compared with the frequency of the incident EM field. Their quasi-free behavior allows them to screen the external EM excitation, preventing considerable penetration of EM fields within the metal. Note that the refractive index, $n = \varepsilon^{1/2}$, is almost purely imaginary in this wavelength range. It is remarkable that even the simple Drude formula reproduces the trend of $\varepsilon(\omega)$ in the near-infrared. At shorter wavelengths ($\lambda \leq 600$ nm), $\mathrm{Re}\{\varepsilon\}$ decreases and $\mathrm{Im}\{\varepsilon\}$, which describes the dissipation of EM energy within the metal, grows due to the presence of interband transitions. The Drude model does not reproduce this increase in metal absorption losses. Including a single Lorentzian correction increases the range of agreement with the experimental data to $\lambda = 400$ nm. Although neither of the two models

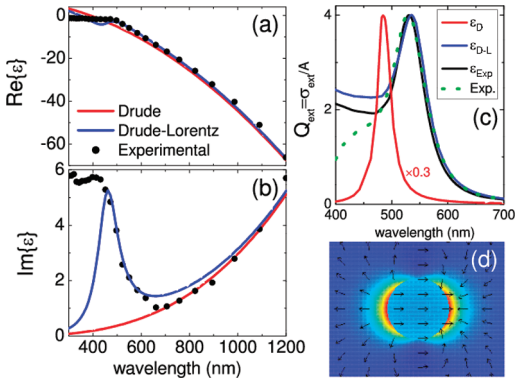


**Figure 2.** (a, b) Real and imaginary parts of the permittivity of gold in the optical regime. Black dots correspond to the experimental data taken from ref 62. The red and blue lines are fits to the Drude and Drude−Lorentz formulas. (c) Extinction cross section for a 25 nm radius gold sphere in water ($\varepsilon_d$ = 1.77). Black line corresponds to theoretical calculations taking the experimental $\varepsilon(\omega)$, and red and blue lines to the Drude and Drude−Lorentz fits, respectively. Green dotted line shows the experimental absorbance spectrum for 25 nm radius colloidal Au nanoparticles in water. (d) Theoretical electric field profile at $\lambda$ = 535 nm for the NP considered in panel c.

reproduces accurately the permittivity of gold at shorter wavelengths, a good comparison with experimental data can be recovered by introducing more than one Lorentzian term in the fitting expression for $\varepsilon(\omega)$.[69−72]

The local approximation of the permittivity of metals fails as the size of the NPs approaches ∼1 nm. This means that a more general nonlocal constitutive relation for the electric fields of the form[73,74]

$$\mathbf{D}(\mathbf{r},\omega) = \varepsilon_0 \int \varepsilon(|\mathbf{r}-\mathbf{r}'|,\omega)\mathbf{E}(\mathbf{r}',\omega)\, dV' \qquad (9)$$

must be considered in order to accurately describe the optical properties of small metal structures. Although we restrict our discussion to the local description of $\varepsilon(\omega)$, nonlocal effects in the dielectric response of metal NPs have been analyzed theoretically using different models for $\varepsilon(|\mathbf{r}-\mathbf{r}'|,\omega)$.[75−77]

The failure of the bulk description of the dielectric properties of metals occurs for NP sizes comparable to the mean free path of conduction electrons. This leads to a spectral broadening of the plasmonic resonances caused by the damping experienced by charge oscillations when scattering with the NP boundaries.[78,79] Finite size effects can be then taken into account through an effective increase of the collision frequency, $\gamma$, in the Drude permittivity. For spherical particles, this can be expressed as

$$\gamma = \gamma_{bulk} + \frac{v_F}{L_{eff}} \qquad (10)$$

where $v_F$ is the Fermi velocity and $L_{eff}$ is the particle diameter.

## 2.3. Localized Surface Plasmon Resonances

Surface plasmon polaritons (SPPs) are transverse magnetic waves propagating along a metal−dielectric interface and evanescently decaying in the direction perpendicular to it.[80,81] SPPs have mixed EM wave and surface-charge nature due to the interaction between light and the collective oscillation of conduction electrons within the metal. The simplest system supporting these confined EM modes is an infinite flat metallic surface. Maxwell's equations provide us with the dispersion relation (frequency versus parallel wavevector) for the plasmonic modes sustained by this geometry

$$k_{||} = k_0\sqrt{\frac{\varepsilon(\omega)\varepsilon_d}{\varepsilon(\omega)+\varepsilon_d}} \qquad (11)$$

where $k_0 = \omega/c$ and $\varepsilon(\omega)$ and $\varepsilon_d$ are the metal and dielectric permittivities, respectively. For simplicity, and without loss of generality, we consider $\varepsilon_d \approx 1$ in our discussion. Using eq 11 and the metal permittivity shown in Figure 2, we can extract the most relevant physical properties of SPPs. At near-infrared wavelengths, $\mathrm{Re}\{\varepsilon(\omega)\} \ll -\varepsilon_d$ and $k_{||} \simeq \varepsilon_d^{1/2}k_0$. This makes the normal component of the SPP wavevector, $k_\perp = (\varepsilon_d k_0^2 - k_{||}^2)^{1/2}$, vanish, and the field amplitude varies very slowly along the direction normal to the metal surface.

At visible wavelengths, the permittivity of noble metals decreases and approaches $-\varepsilon_d$. This causes the real part of the denominator in eq 11 to vanish, yielding $\mathrm{Im}\{k_\perp\} \gg \varepsilon_d^{1/2}k_0$. EM fields then experience a fast decay along the normal direction into the dielectric material (note that $\mathrm{Im}\{k_\perp\}$ is inversely proportional to the SPP normal decay length). This leads to the concentration of EM energy into subwavelength volumes at the surface of the metal and overcomes one of the main constrains of classical optics, the diffraction limit.[63] The striking ability of SPPs to guide and confine light into the subwavelength scale has been the focus of much attention during the past decade in the context of nanophotonics research.[82−86]

Flat surfaces are not the only geometry where plasmonic modes arise. The fingerprint of these peculiar EM modes can easily be recognized in the polarizability, $\alpha_p$, of a spherical metallic NP. $\alpha_p$ is defined as the ratio between the dipole moment induced in the NP by an incoming wave and the amplitude of the incident displacement field ($\alpha_p = \mu/(\varepsilon_0\varepsilon_d\mathbf{E}_0)$). For a NP with radius, $R$, much smaller than the effective wavelength, $\lambda/\varepsilon_d^{1/2}$, retardation effects can be neglected. The electrostatic (Rayleigh[10]) approximation yields an accurate expression for the polarizability[87]

$$\alpha_p = 4\pi R^3\frac{\varepsilon(\omega)-\varepsilon_d}{\varepsilon(\omega)+2\varepsilon_d} \qquad (12)$$

In a similar way to what happens for $k_{||}$ in the flat geometry, $\alpha_p$ grows for smaller metal permittivities, diverging for frequencies satisfying $\varepsilon(\omega) = -2\varepsilon_d$. By comparison with the flat geometry, this result can be interpreted as the appearance of resonances in the NP dielectric response at incident wavelengths matching those of the plasmonic modes supported by the NP. For this reason, plasmonic effects in metal NPs are usually termed localized surface plasmon resonances (LSPRs). Although the validity of eq 12 is restricted to spherical geometries in the electrostatic regime, the formation of LSPRs in metal particles of arbitrary shape and size is revealed by full electrodynamic calculations based on analytical[12,13] or numerical approaches.[88−99]

The link between $\alpha_p$ and the NP extinction cross section is provided through the Optical Theorem. It can be demonstrated[57] that for small spherical particles, $\mathbf{f}(\mathbf{n},\mathbf{n}_0) = [(\varepsilon_d^{1/2}k_0)^3/(4\pi)]\mathbf{n}\times(\mathbf{n}\times\alpha_p\mathbf{e}_0)$. Equation 6 then yields

$$\sigma_{ext} = \sqrt{\varepsilon_d}k_0\mathrm{Im}\{\alpha_p\} \qquad (13)$$

for particles whose radius is much smaller than the incoming wavelength. All the EM energy removed by the incoming radiation in the scattering process is lost in the form of work performed by the incident electric field on the dipole moment induced in the NP.

Figure 2c shows the extinction cross sections normalized to the physical cross section ($Q_{ext} = \sigma_{ext}/A$) for a 25 nm radius gold NP. The spectra, plotted in black, red, and blue, were calculated using Mie theory and dielectric data for gold from Johnson and Christy,[62] and the Drude and Drude−Lorentz models shown in panels a and b. For comparison, the normalized experimental absorbance spectrum measured using 50 nm spherical gold colloids is plotted as the green dotted line in Figure 2c. In both experiment and simulations, the gold particles are embedded in water ($\varepsilon_d = 1.77$). There is an excellent agreement between the position of the spectral features obtained in the experiment and calculations for the Johnson and Christy and Drude−Lorentz permittivities. However, the Drude model leads to a blue shift, narrowing, and increase of the cross section. These effects are related to the failure of the Drude model at short wavelengths, where it underestimates both the real and imaginary parts of $\varepsilon(\omega)$.

The nature of the LSPR responsible for the cross section peak observed at $\lambda = 535$ nm in Figure 2c is revealed by the scattered electric field, $\mathbf{E}_{sca}$, shown in panel d. The color contour plot shows the time averaged field amplitude, and the arrows indicate the instantaneous orientation of $\mathbf{E}_{sca}$ at resonance. This field profile resembles that of an oscillating electric dipole.[58] This enables us to identify the dipolar character of the plasmonic mode causing the extinction maximum. At resonance, the charges induced by $\mathbf{E}_{inc}$ oscillate coherently within the NP along the direction of polarization in a similar way to an oscillating electric dipole. This effective charge oscillation gives rise to the dipole-like electric field map shown in Figure 2d. It is remarkable that $Q_{ext} = 4$ at resonance, and $\sigma_{ext}$ for the NP is four times larger than its physical cross section. This means that the interception area that the spherical particle presents to the incident radiation is much larger than its actual size. As we will see in the following section, this enlargement of the effective cross section of metal NPs caused by LSPRs allows us to consider them as optical antennas (or nanoantennas), due to their strong interaction with incoming light.

### 2.4. Optical Nanoantennas

We have seen how the excitation of LSPRs effectively increases the size of Au nanospheres interacting with free space radiation. This plasmonic effect is not restricted to gold spheres but takes place in any metallic NP. Figure 3a shows the absorption (solid lines) and scattering (dashed lines) efficiencies ($Q = \sigma/A$) of two different silver NPs of similar dimensions, a cube and a ring. Each side of the cube is 50 nm, the outer and inner diameters of the ring are 50 and 30 nm, respectively, and its height is 20 nm. The structures are illuminated from the top by a linearly polarized plane wave. In both cases, the normalized cross sections present a maximum within the visible range, which is linked to the excitation of dipolar LSPRs. For the two NPs considered, only a small part of the incident energy is scattered and absorption dominates the cross section. This is the case for metal particles much smaller than the wavelength (sizes ~50 nm or less for gold and silver), whereas for larger sizes, it is the scattering contribution that dominates the cross section.

Figure 3a demonstrates that shape affects the properties of LSPRs supported by metal NPs, including the height and width of the cross section maxima. The cubic NP presents a broad peak around $\lambda = 430$ nm (violet part of the EM spectrum), whereas in the ring, the peak is narrower and shifted to ~568 nm (in the green-yellow part of the spectrum). At resonance, NPs not only absorb but also scatter light much more efficiently than at any other wavelength. Therefore, the cubic (ring) NP considered in Figure 3a scatters efficiently in the violet (green) when illuminated by white light. Remarkably, in both cases, the extinction cross section of the NP becomes several times larger than its actual size at resonance. This, together with their spectrally narrow response, makes metal NPs good candidates for nanoantennas.

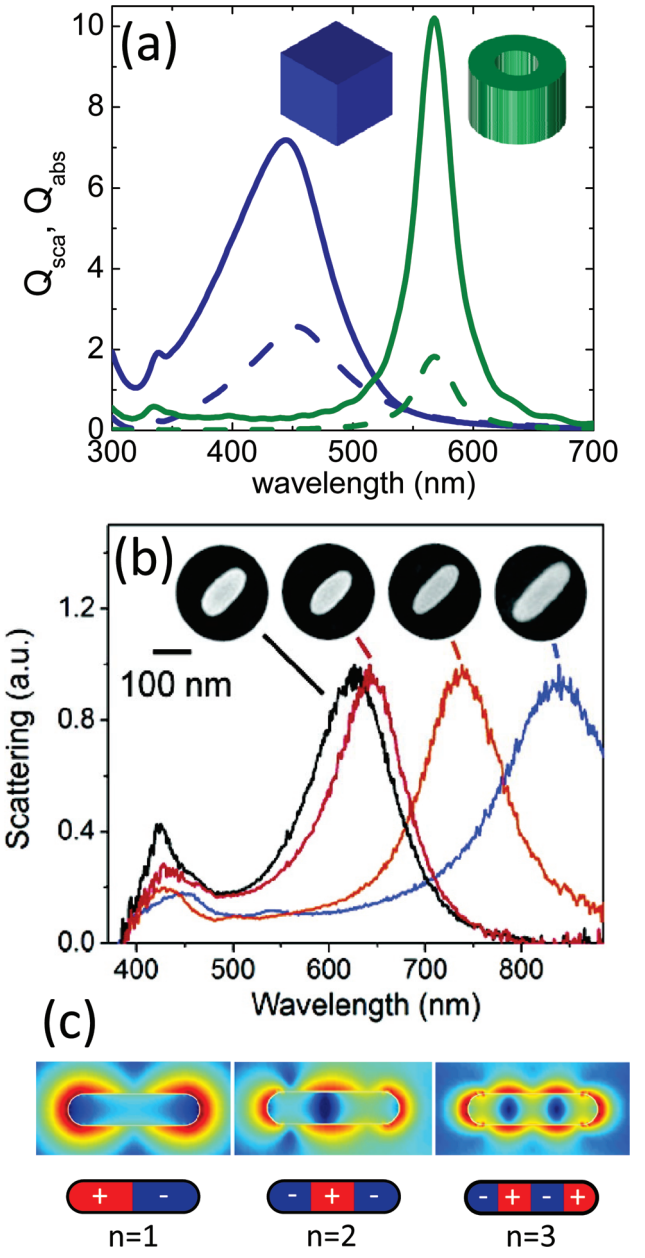


**Figure 3.** (a) Calculated absorption (solid lines) and scattering (dashed lines) efficiencies for a cubic (blue) and a ring (green) shaped silver NP. The particles have similar dimensions, both the side of the cube and the diameter of the ring are 50 nm. (b) Experimentally measured scattering spectra of silver nanobars of length 100−200 nm. The height and width of the particles, shown in the insets of the panel, are 55 and 50 nm, respectively. Adapted with permission.[103] (c) Electric field intensity enhancement corresponding to the three lowest longitudinal LSPRs supported by 400 nm long Ag NPs of 50 × 100 nm$^2$ cross section. Color code: the field amplitude on a logarithmic scale from 0.1 (blue) to 100 (red). The bottom sketches show the instantaneous charge distributions for the three plasmonic resonances.

Elongated NPs offer a new degree of freedom in tailoring the optical properties of metallic structures.[47,100] The anisotropic shape of such particles enables them to support resonant plasmonic modes at different spectral positions,[101,102] associated with induced charge oscillations along their different symmetry axes. This effect is illustrated in Figure 3b, which shows normalized scattering spectra for chemically synthesized single Ag nanobars placed on top of a glass substrate. The height and width of the particles is fixed at 50 and 55 nm, respectively, and their length is varied from 100 to 200 nm. The insets show scanning electron microscope (SEM) images of the four NPs considered. The measured spectra were obtained for unpolarized incident light. They show two peaks, one fixed at $\lambda = 430$ nm and another whose position changes from the visible (~620 nm) to the near-infrared (~850 nm) depending on the NP aspect ratio. The former is linked to the excitation of LSPRs in which induced charges move back and forth along the short axis (width) of the particle, which remains fixed for all samples. The latter is due to plasmonic modes leading to charge oscillations along the long axis (length) of the particle, and therefore, its position red shifts with increasing NP length. As expected, the scattering peaks associated with longitudinal LSPRs are larger than those for transversal resonances, as they lead to a larger effective cross section of the metal NP. Figure 3b demonstrates how elongated metallic NPs are able to scatter light efficiently at various wavelength ranges (visible and near-infrared) and how the position and height of the cross section maximum can be modified by changing the NP aspect ratio.

An efficient antenna must not only have a large and spectrally tunable cross section but also give rise to a large local field enhancement.[44] In the following, we show that elongated NPs, like those considered in Figure 3b, are potentially good nanoantennas.[103] As we have seen, the optical response of metal nanobars is mainly controlled by the length ($L$) of their axis parallel to the incident electric field. In a phenomenological picture, we can describe the NP as a Fabry−Pérot cavity, whose resonances will be given by $\sin(k_{\mathrm{eff}}L) = 0$, where $k_{\mathrm{eff}} = 2\pi/\lambda_{\mathrm{eff}}$ is the mode wavevector along the direction of polarization. This approximate relation can be rewritten as

$$L = \frac{n}{2}\lambda_{\mathrm{eff}} \tag{14}$$

where $n$ is any integer number. Equation 14 forces the effective wavelength of the LSPR to fit exactly a half-integer number of times into the NP length. The validity of this simple rule is verified in Figure 3c, which shows the calculated field enhancement, $|E|^2/|E_0|^2$, surrounding a gold nanobar with dimensions $400 \times 100 \times 50\ \mathrm{nm}^3$ for its three lowest LSPRs. The NP is placed on top of a glass substrate and is illuminated from the top by a plane wave tilted 20 with respect the vertical direction and polarized along its long axis. The color code for the enhancement is from 0.1 (blue) to 100 (red). The free space resonant wavelengths for the three LSPRs are, from left to right, $\lambda$ = 1375, 770, and 630 nm. The three bottom sketches show how eq 14 is satisfied in the system and indicate the value of $n$ for each plasmonic resonance.

The lowest and most intense LSPR ($n = 1$) supported by metal nanobars fulfills $L = \lambda_{\mathrm{eff}}/2$ (half-wave resonance). The corresponding electric field, shown in the left panel of Figure 3c, has a maximum at the ends of the bar outside the metallic NP. The induced charges, given by the divergence of the electric field, follows the dipolar distribution we have already predicted. These simple arguments hold for higher order resonances, such as those corresponding to $n = 2$ and 3 in Figure 3c. It is remarkable that the excitation of LSPRs in simple nanoantenna geometries such as the nanobar leads to field enhancements of around 100 close to the metal particle.

We have not yet established a link between the free space wavelength of the incoming light, $\lambda$, and the effective wavelength of the plasmonic mode, $\lambda_{\mathrm{eff}}$, supported by the NP. As mentioned above at radio and telecom frequencies, the high permittivity of metals prevents the penetration of external EM signals into them. This means that the relation between $\lambda$ and $\lambda_{\mathrm{eff}}$ is completely governed by geometry in conventional antennas. However, at higher frequencies, the dielectric function of metals is lower (in absolute value) and EM fields can penetrate deeper into the metal. This leads to the excitation of plasmonic modes by the incident light and translates into an increase of the effective wavevector of the incoming photons, as demonstrated for a flat surface by eq 11. Therefore, at visible frequencies, the relation between $\lambda$ and $\lambda_{\mathrm{eff}}$ is controlled not only by the shape of the nanoantenna but also by intrinsic plasmonic effects related to the dielectric properties of the metal structure and its surroundings. Using a simple model based on a metal cylindrical waveguide, Novotny[104] demonstrated that the scaling law for the effective wavelength in optical antennas can be expressed as

$$\lambda_{\mathrm{eff}} = n_1 + n_2\frac{\lambda}{\lambda_{\mathrm{p}}} \tag{15}$$

where $\lambda_{\mathrm{p}} = 2\pi c/\omega_{\mathrm{p}}$ is the plasma wavelength, and $n_1$ and $n_2$ are parameters that depend on both the geometry and the dielectric properties of the system. This expression accounts for the increase in momentum experienced by incident photons as a result of their interaction with a metal NP for an incoming wavelength approaching $\lambda_{\mathrm{p}}$.[44] Note that eq 15 has the same form as eq 11 for the particular case of planar metal−dielectric interfaces.

As we have already stated, a good nanoantenna is characterized by a large cross section and a large near-field enhancement. The former enables it to collect EM energy from the incident radiation with high efficiency. The latter allows the transfer of most of that energy into small volumes in the vicinity of the nanoantenna. A successful strategy to increase the performance of a nanobar optical antenna consists of cutting it at its middle, thereby opening a gap along its long axis. This improves the field enhancement capability of the structure without a considerable reduction of its effective cross section. The effect of opening a gap in elongated nanoantennas has been studied by Ghenuche et al.,[107] who measured the two-photon luminescence (TPL, see section 3), see section 3 maps for three different gold nanoantennas on top of a glass substrate at $\lambda = 730$ nm (see Figure 4). Note that TPL is proportional to the local electric field intensity, $|\mathbf{E}|^2$. The SEM images of the three structures, whose height and width are fixed at 50 and 100 nm, respectively, are also shown. Panel a shows the field distribution for a single 500 nm long nanobar, which has a maximum at the ends of the structure similarly to the left panel of Figure 3c. This indicates that a half wavelength LSPR is excited in the system. Panel b corresponds to a composite antenna comprising two 500 nm long nanobars separated by a 40 nm gap. The plasmonic resonance leads to a much larger field enhancement concentrated at the gap of the antenna. This is illustrated by considering the TPL map measured for a 1 $\mu$m nanobar and plotted in Figure 4c. The system is out of resonance, and the

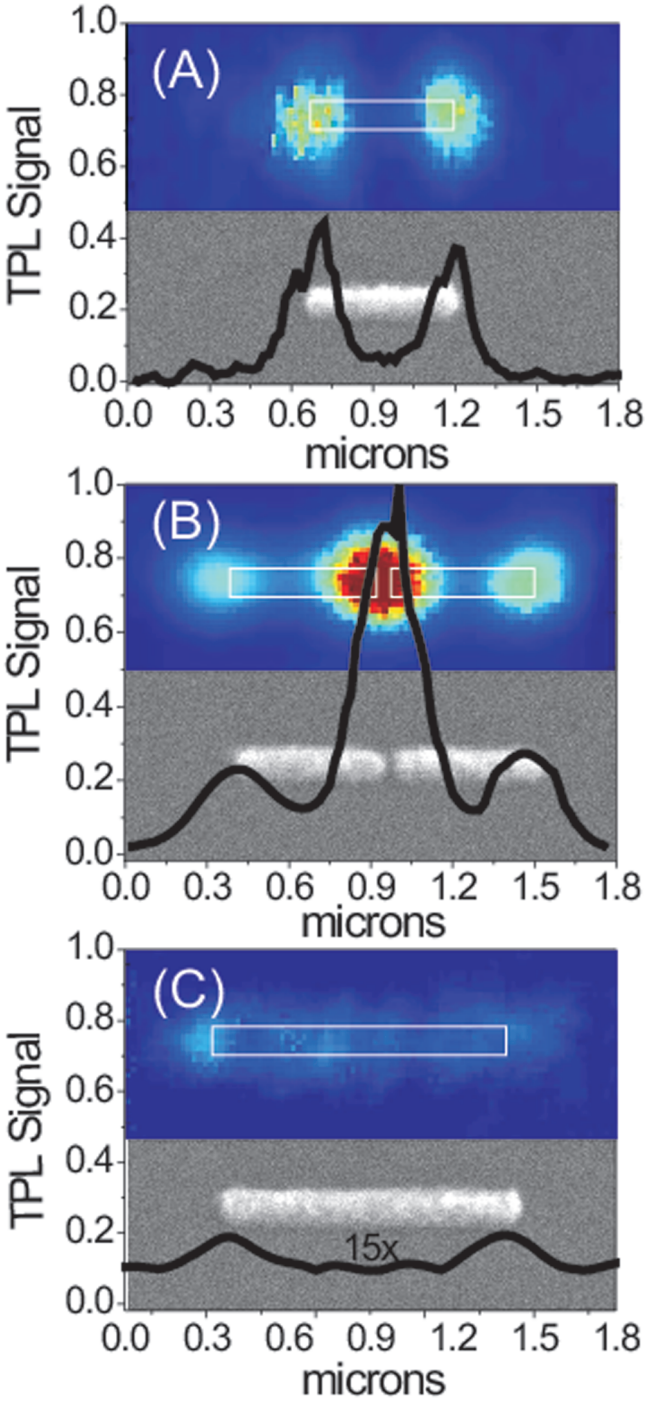


**Figure 4.** TPL scans for three different gold nanoantennas and their respective SEM images: (A) a single 500 nm long bar, (B) two coupled 500 nm long bars separated by a 40 nm gap, and (C) a 1 $\mu$m long bar. The height and width of the antennas is fixed to 50 and 100 nm, respectively. The superimposed black lines plot the TPL signal along the symmetry axis of the antennas. The incident polarization is parallel to the long antenna axis, and all the measurements were performed at $\lambda$ = 730 nm, for which the gap antenna (B) is at resonance. Adapted with permission.[107] Copyright 2008, American Physical Society.

enhancement is drastically reduced in comparison with the two previous structures. This shows that the resonant properties of the composite antenna in Figure 4b are controlled by the LSPRs supported by each of the arms and their coupling through the antenna gap,[105] rather than by the plasmonic modes of a gapless antenna with the same overall length. This result anticipates the plasmon hybridization concept,[106] which will be discussed in the following section.

We can gain insight into the electric field concentration that takes place in composite nanoantennas by thinking of the gap as a capacitor. The electric field amplitude between the internal walls of the arms of the antenna is mainly governed by its longitudinal component and must be uniform.[58] The continuity condition on the normal components of the displacement field at the gap walls then provides us with the relation between the field amplitude in the gap, $|\mathbf{E}_{gap}|$, and inside the antenna arm, $|\mathbf{E}_{arm}|$,

$$\frac{|\mathbf{E}_{gap}|}{|\mathbf{E}_{arm}|} = \frac{\varepsilon(\omega)}{\varepsilon_d} \tag{16}$$

$\varepsilon(\omega)$ and $\varepsilon_d$ are the permittivity of the metallic nanoantenna and the dielectric medium filling the gap, respectively. Note that eq 16 is a crude description of the field concentration taking place at nanoantenna gaps, because it does not take into account the coupling of the fields in each arm of the antenna through the gap. These effects lead to intensity enhancements larger than $10^3$ in metal composite nanoantennas operating at visible frequencies with gaps of a few tens of nanometers in size. Therefore, tailoring of the gap geometry and filling it with dielectric materials provide new strategies to tune the EM response of nanoantennas, as recently demonstrated experimentally.[108,109]

Although, for simplicity, we have focused our discussion on bar-shaped NPs, many other nanoantenna geometries have been analyzed both experimentally and theoretically. The range of nanoantenna configurations explored in the literature covers complex shaped individual NPs such as discs,[110] triangles,[111] prisms,[112] rings,[113] stars,[114] or flowers,[41] as well as composite antenna geometries such as dimers,[42,115] bowties,[116] trimers,[42,117] dolmens,[55] or quadrumers.[118]

### 2.5. Dark Modes and Fano Resonances

Although metal NPs sustain plasmonic resonances with different symmetry properties, the strong radiative character of dipolar charge oscillations means that the interaction of nanoantennas with free space radiation is mainly controlled by dipole LSPRs. For this reason, these plasmonic modes, which are the lowest in energy, are also termed bright modes.[59] Note that this is a well-known fact that we have already exploited in eq 13, where we described the scattering properties of deeply subwavelength metal particles through their electrostatic dipolar polarizability. However, larger metal structures support higher multipole resonances, which couple very weakly to radiation. These higher order LSPRs are labeled as dark modes. Importantly, the only mechanism that permits the optical excitation of multipole resonances is retardation effects within the nanoantenna. These are related to the slow response (in comparison to the incoming frequency) of the metal's conduction electrons to the external EM excitation and lead to a phase mismatch between the incident fields and the effective charge oscillations within the nanoantenna.

The normalized scattering intensity measured from a single 200 nm side Ag triangular nanoprism using white light dark field microscopy is plotted in Figure 5a.[119] The insets show the SEM images of the NPs considered in the experiments, and the scale bar corresponds to 200 nm. The spectrum is dominated by a broad maximum around 670 nm, the origin of which is the bright dipole resonance that the NP supports at low frequencies.

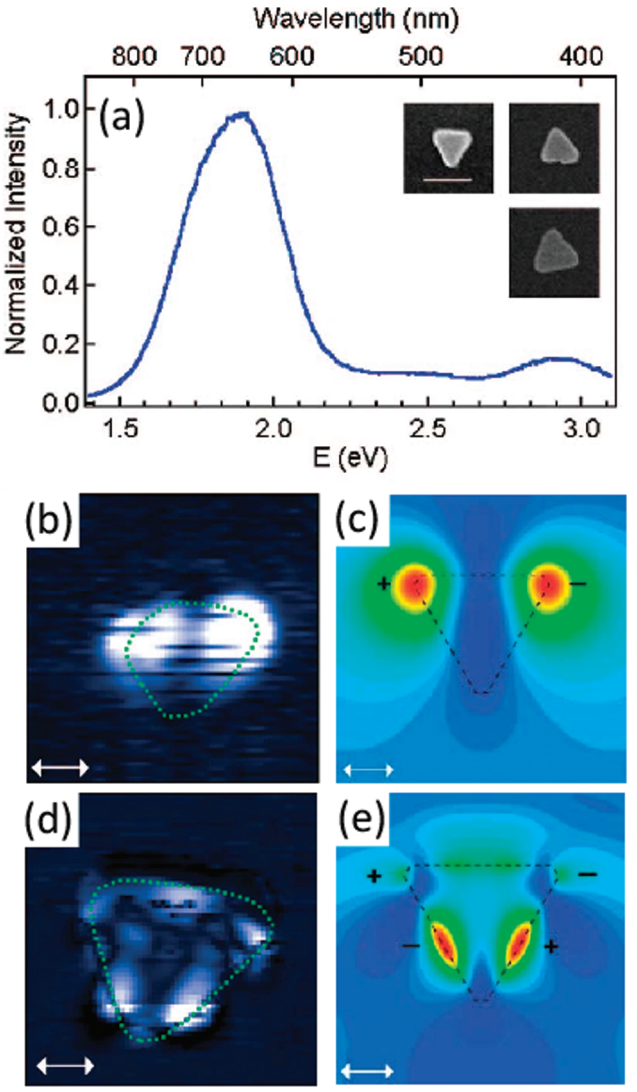


**Figure 5.** (a) Normalized scattering spectra of an isolated silver nanoprism. Inset: SEM images of the structures under consideration (scale bar, 200 nm). (b, c) Theoretical and experimental electric field distributions, respectively, for nanoprisms supporting a dipole LSPR. Panels d and e are identical to panels b and c but for a larger NP under quadrupole excitation. Arrows indicate the polarization of the incident light ($\lambda$ = 632 nm). Adapted with permission.[119]

However, at larger photon energies ($\lambda \simeq 430$ nm), the scattering intensity shows a bump, which can be associated with the excitation of a dark quadrupole LSPR in the structure. The use of a scanning near-field optical tip enables the probing of the various components of the resonant evanescent fields at the NP. The near-field pattern obtained for a 120 nm nanoprism exhibiting a dipole plasmonic resonance is shown in Figure 5b. The profile plotted in Figure 5d corresponds to a larger NP, whose optical response at the same frequency as panel b is dominated by the excitation of a quadrupole LSPR. The experimental identification of the nanoprism plasmonic modes is supported by calculations. Panels c and e show theoretical field distributions for the dipole and quadrupole resonances measured in the experiment and signs indicate the relative phase of the resonant fields. For all the field plots in Figure 5, $\lambda$ = 632 nm, and arrows indicate the polarization of the incident light.

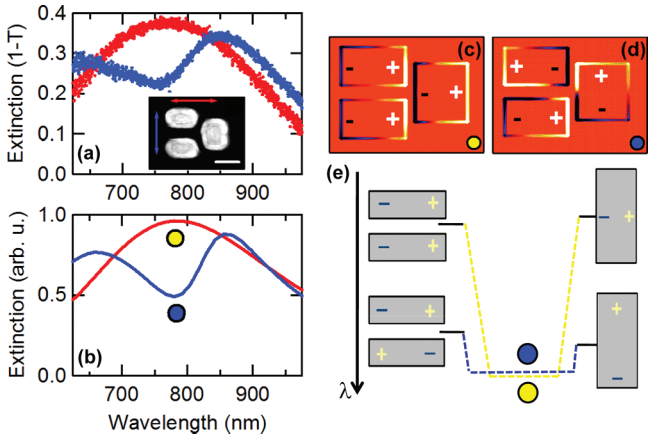


**Figure 6.** (a) Confocal extinction spectra for the dolmen nanoantenna shown in the inset of the panel. The structure (200 nm side) is illuminated by light with different polarizations (red and blue arrows). (b) Theoretical extinction cross sections of the nanoantenna computed by finite-difference time-domain (FDTD) simulations. (c, d) Induced charge distribution in the dolmen under the two polarizations at the wavelengths indicated by yellow and blue dots in panel b. (e) Hybridization diagram for the two plasmonic resonances shown in panels c and d. Adapted with permission.[123]

A deeper understanding of bright and dark plasmonic modes can be achieved by analyzing the optical properties of composite nanoantennas in which a NP sustaining a quadrupole mode is placed in the near-field of another exhibiting a dipole resonance. The dark nature of the former makes it spectrally narrow, as its width is only controlled by absorption effects within the metal. On the other hand, the latter presents a broad spectral character, as it suffers from strong radiative damping. In the time domain, this means that resonant fields corresponding to bright (dark) modes spend a little (long) time before being reradiated (absorbed) by the metallic NP. When these different plasmonic resonances interact, asymmetric spectral profiles arise. In analogy to the features observed in atomic autoionization spectra, they are termed Fano resonances.[120−122] These consist of spectral peaks and dips, very close in frequency, that originate from the constructive and destructive interference of narrow (dark) and broad (bright) NP resonances.

Figure 6 shows the experimental (a) and theoretical (b) extinction spectra for a dolmen-shaped nanoantenna. It is composed of three gold nanobars of similar dimensions (100−200 nm, see inset) and supports a Fano resonance in the infrared regime.[123] We consider first the response of the structure when it is illuminated from the top with light polarized along the long axis of the dimer formed by the two parallel nanobars (red arrow). In this configuration, the extinction spectrum (in red in both panels) shows a broad maximum around 780 nm (yellow circle). This peak can be attributed to the constructive superposition of the longitudinal dipole resonance excited in the dimer with the transverse dipole mode in the perpendicular monomer. This is clarified in panel c, which shows the induced charge distributions calculated at $\lambda$ = 780 nm for this case. When the incident polarization is rotated 90 degrees (blue arrow), measured and calculated spectra (in blue) develop a narrow dip at the same wavelength (blue circle). This yields an asymmetric spectral profile, fingerprint of the formation of a Fano resonance in the system. The physical origin of this Fano resonance is revealed by the charge distribution plotted in panel d. It demonstrates that the


dx.doi.org/10.1021/cr1002672 |*Chem. Rev.* 2011, 111, 3888–3912

extinction minimum results from the destructive interaction between the bright longitudinal dipole mode of the monomer and the dark quadrupole resonance excited in the dimer. It is important to notice that this quadrupole mode could never be excited by normally incident light and that it is the presence of the monomer that allows its near-field excitation.

An ingredient needed for the appearance of Fano resonances in composite nanoantennas is structural asymmetries. This allows the coupling between bright and dark plasmonic modes supported by its closely spaced constituents. Fano resonances have been recently explored as a means to tune the spectral response of nanoantennas.[124−127] Remarkably, it has been demonstrated that the tailoring of Fano resonances can lead to sharp and deep extinction minima. This makes the supporting nanostructure *transparent* to incoming radiation within a narrow frequency range. In analogy to its atomic version,[128] this effect is known as plasmonic-induced optical transparency and has been recently predicted theoretically[35] and verified experimentally.[129]

The hybridization model[106] is an elegant theoretical approach that provides physical insight into the interaction of LSPRs supported by closely spaced NPs. Although the model was first developed for dimers of spherical particles, the underlying ideas can be transferred to any geometry.[130] The model establishes the analogy between bound plasmonic modes in metal NPs and electronic orbitals in covalent molecules. Molecular orbitals emerge from the overlapping of the atomic orbitals. In a similar way, LSPRs of composite metal structures result from the evanescent EM coupling between the modes supported by their isolated components. In the case of spherical NP dimers, the model enables us to write the following electrostatic Lagrangian for the dynamics of the surface charge deformations at each particle:[131]

$$L = \sum_{i,j} \left\{ \left[ \left( \frac{\mathrm{d}S_i}{\mathrm{d}t} \right)^2 - \omega_i^2 S_i^2 \right] \delta_{ij} - V_{ij}(d) S_i S_j \right\} \qquad (17)$$

$S_i$ are the deformation amplitudes of the NP surface charge, $\sigma(\Omega,t) = \Sigma_i S_i(t) Y_i(\Omega)$, expressed in terms of spherical harmonics, $Y_i(\Omega)$[132] (where $\Omega$ is the solid angle measured from the NP center). The diagonal terms in eq 17 describe the charge oscillations for each NP, and $\omega_i$ denote the eigenfrequencies of the various LSPRs supported by them when isolated from the rest of the system. The nondiagonal part of the Lagrangian takes into account the electrostatic interaction between the NPs, and $V_{ij}(d)$ (where $d$ is the interparticle distance) is the projection of the Coulomb interaction onto a spherical harmonics basis.

Panel e of Figure 6 shows a schematic diagram based on the plasmon hybridization model for the two plasmonic resonances excited in the dolmen nanoantenna. It shows how the coupling of the different LSPRs, supported by the isolated monomer and dimer components, leads to the formation of a bright and a dark mode in the overall system at the same energy. Thus, depending on the incident polarization, which selects the excited plasmonic resonance in the structure, the extinction cross section of the dolmen-shaped antenna can develop a maximum (yellow circle) or a minimum (blue circle) at the same wavelength.

Recently, theoretical studies on nanoantenna configurations containing geometric singularities, such as crescents or cylindrical and spherical particles touching at a single point, have demonstrated a large absorption cross section (on the order of the physical size) over a large spectral window. Moreover, remarkable field enhancements have been predicted in these nanoparticle geometries, where EM fields accumulate as they propagate toward the structure singularity.[133−137]

### 2.6. Nanoparticle Arrays

We have studied above the LSPRs sustained by individual NPs, and we have analyzed how they interact when a number of NPs are placed in close proximity, leading to the formation of hybrid plasmonic modes supported by the resulting structure as a whole. We previously restricted our discussion to nanoantennas comprising a small number of elements but did not explore the optical properties of arrays of NPs.

When light is incident on a two-dimensional array of metal particles, it is scattered by different elements in the structure. The presence of order in the system enables the appearance of coherent effects among the various scattered waves. Bloch's theorem[138] provides us with the relation between the in-plane wavevector for the various diffraction orders, $\{m,n\}$, and the geometry of the structure

$$\mathbf{k}_{mn} = \mathbf{k}_{\mathrm{inc}} + m\frac{2\pi}{d_1}\mathbf{u}_1 + n\frac{2\pi}{d_2}\mathbf{u}_2 \qquad (18)$$

where $\mathbf{k}_{\mathrm{inc}}$ is the in-plane wavevector for the incident plane wave and $d_1$ ($d_2$) is the array pitch along the direction of the unit vector $\mathbf{u}_1$ ($\mathbf{u}_2$).

At normal incidence ($\mathbf{k}_{\mathrm{inc}} = 0$), the lowest order coherent superposition of the incoming and scattered fields occurs when the wavelength of the incident light is similar to the pitch of the array. This gives rise to collective EM resonances of the metallic NPs, which are spectrally very narrow due to their extended spatial character. The associated EM fields can travel many wavelengths within the structure before being scattered. These phenomena are similar to the Rayleigh's and Wood's anomalies observed when light is diffracted by metallic gratings.[139,140] The condition for the occurrence of Rayleigh's anomaly under an arbitrary angle of incidence can be written as

$$|\mathbf{k}_{nm}| = k_0 \qquad (19)$$

which implies that all the momentum of the scattered radiation is parallel to the plane of the array (note that the normal wavevector vanishes if eq 19 is satisfied). This transforms the scattered fields into grazing waves, which travel along the structure for many periods without being radiated back into the free space. The hybridization of these grazing waves with LSPRs gives rise to collective NP resonances. This enables us to drastically modify the optical properties of metal NPs by designing arrays in which geometric effects take place near the spectral position of LSPRs. This phenomenon was predicted theoretically a long time ago,[141−144] and it has recently been demonstrated experimentally.[145−149]

The coupled dipole approximation[150] enables us to describe how array resonances affect the optical properties of individual NPs. This is done by calculating[151] the effective polarizability of spherical NPs in the array, obtaining

$$\alpha_{\mathrm{p}}' = \frac{\alpha_{\mathrm{p}}}{1 - \alpha_{\mathrm{p}} S} \qquad (20)$$

where $\alpha_{\mathrm{p}}$ is the polarizability of the isolated NP, given by eq 12 for small spherical particles. The factor $S$ reflects the contribution to the dipole induced in the NP by EM fields scattered by the rest

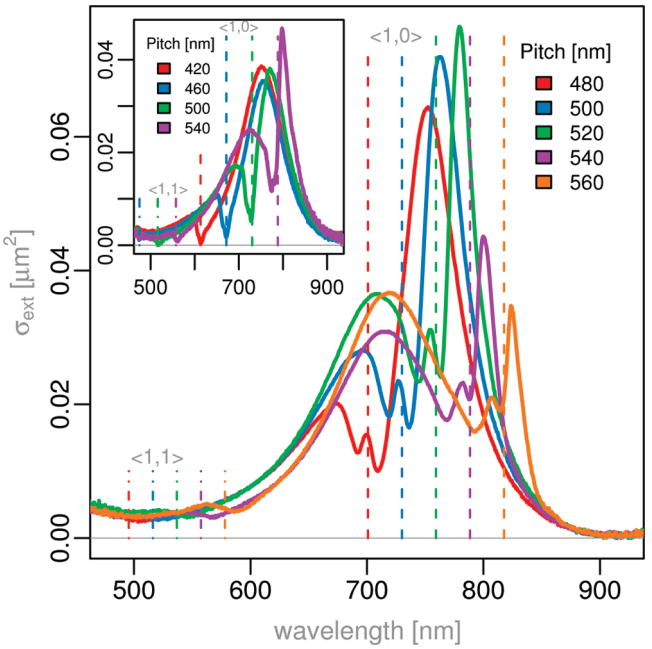


**Figure 7.** Measured extinction spectra (per particle) for several gold NP arrays. The average particle size is 123 × 85 × 35 nm$^3$. Inset: Measured extinction spectra for particles of size 120 × 90 × 35 nm$^3$. Adapted with permission.[145] Copyright 2008, American Physical Society.

of the array. For infinitely periodic arrays, this parameter can be written as

$$S = \sum_{i \neq j} \left[ \frac{(1 - i\sqrt{\varepsilon_d} k_0 r_{ij} - 1)(3\cos^2\theta_{ij} - 1)}{r_{ij}^3} + \frac{\varepsilon_d k_0^2 \sin^2\theta_{ij}}{r_{ij}} \right] e^{i\sqrt{\varepsilon_d} k_0 r_{ij}} \quad (21)$$

where $r_{ij}$ is the distance between NP $i$ and $j$ and $\theta_{ij}$ is the angle between $\mathbf{r}_{ij}$ and the polarization direction.

A clear experimental demonstration of the excitation of collective modes was shown by Auguié et al.[145] They measured the extinction spectra from gold NPs arranged in a 35 $\mu$m square periodic array; the results are plotted in Figure 7. The nominal dimensions of the particles are 123 × 85 × 35 nm$^3$ and 120 × 90 × 35 nm$^3$ (inset), and the pitch of the arrays ranges from 420 to 560 nm. The vertical dashed lines in Figure 7 indicate the position of the edges given by eq 19 for the first diffraction orders, {1,0} and {1,1}.

In the extinction spectra of the main panel of Figure 7, we observe a broad feature at $\lambda$ = 710 nm, which is due to the excitation of a dipolar LSPR in the NPs. A set of narrow peaks, which shifts to longer wavelengths as the period of the structure is increased, is also shown. These features are related to the excitation of collective resonances in the system and are given by the zeros of the real part of the denominator in eq 20, that is, $\mathcal{R}(1 - \alpha_p S) = 0$. From the dependence of $\sigma_{ext}$ on the array period shown in Figure 7, two different regimes can be identified. When the lowest diffraction edge lies at a shorter wavelength than the individual LSPR (inset), the spectra develop sharp dips. These originate from the reduction in the radiative coupling of the plasmonic resonances supported by the NPs. In this regime, all diffraction orders are evanescent at 710 nm. When the diffraction edge is at a longer wavelength than the individual

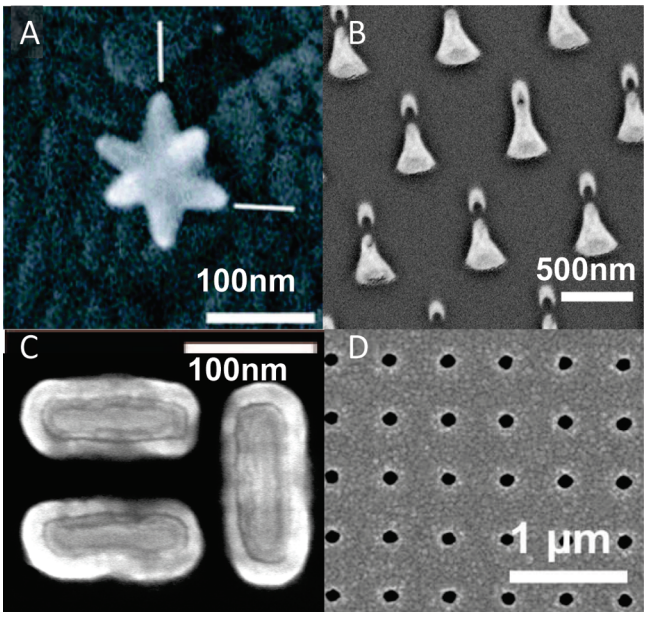


**Figure 8.** The top row shows metal nanoparticles made by bottom-up approaches, while those in the bottom row are fabricated by top-down methods: scanning electron microscope image of (A) a colloidal gold nanostar, adapted with permission,[17] (B) a hexagonally arranged array of Au nanoshuttlecocks obtained by colloidal lithography, adapted with permission,[159] (C) a dolmen-type resonator fabricated via electron beam lithography and ion milling, adapted with permission,[123] and (D) a silver grating fabricated using thermal nanoimprint lithography and shadow evaporation, adapted with permission.[160] Copyright 2008, IEEE.

LSPR (main panel), very sharp and intense peaks appear in the long wavelength tail of the individual resonances. The intensity and width of these peaks decrease as they shift to longer wavelengths. In this case, the array resonances increase the radiative character of the plasmonic resonances of the individual NPs.

Thus, by arranging metallic NPs in a periodic fashion, we can modify their far-field properties and tune their optical responses. Importantly, and although it is outside of the scope of this discussion, NP arrays can also enable the concentration and guiding of light at subwavelength scales.[152−154] Recently, the emission enhancement of dye molecules (see section 4) assisted by collective dipolar or multipolar resonances in arrays of NPs has been also reported.[148,155]

## 3. FABRICATION AND CHARACTERIZATION

Over the last number of decades there have been huge developments in the fabrication of metallic nanostructures. Such structures can be on the order of 100 nm or less and can be fabricated in a bottom-up or top-down approach.[158]

Bottom-up fabrication processes include the chemical synthesis of NPs, which enables the production of large numbers of NPs in a range of sizes and shapes, including spheres, cubes, rods, octahedrons, triangular prisms, boxes, and stars.[17,49,103,161−165] The synthesis involves the reduction of metal salts by a chemical agent[162] or by photochemical processes.[165−167] Once the reduction is complete, further chemistry can be carried out including galvanic replacement reaction.[49] Synthesized NPs can remain as colloids or be deposited on a substrate,[168] as can be seen in the top left panel of Figure 8.[17] There are also reports of metal NP

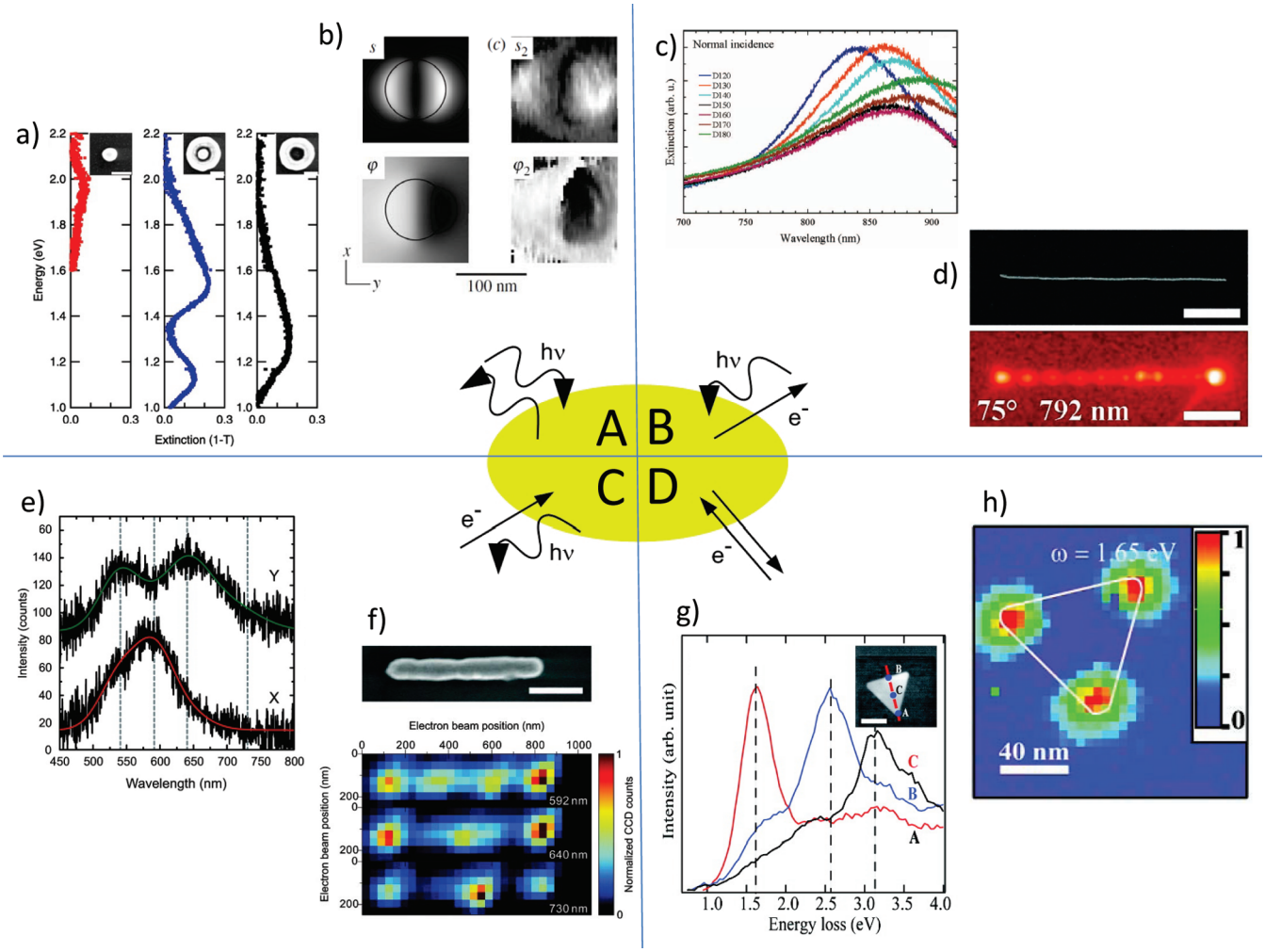


**Figure 9.** Four types of measurement techniques (A−D) used to study plasmons:[185] In the top row, plasmons are excited by photons (A, B), while in the bottom row, (C, D) plasmons are excited by the electromagnetic field associated with an electron beam: (a) Confocal microscopy extinction spectra for a disk, a ring, and a concentric disk and a ring. Adapted with permission.[127] (b) Comparison between theoretical and experimental phase and amplitude SNOM images supported by a metal disk. Adapted with permission.[186] Copyright 2004, F. Keilmann. (c) Extinction spectra for a square array of disk-shaped Au particles with a diameter range between 120 and 180 nm. Adapted with permission.[223] Copyright 2007, American Institute of Physics. (d) Top panel, SEM image of a 4 $\mu$m long nanowire; bottom panel, photoemission electron microscopy near-field mapping. Adapted with permission.[187] (e) Cathodoluminescence spectra taken at two different positions (*X* and *Y*) along a 725 nm long Au nanowire. Adapted with permission.[188] (f) Top panel, SEM image of the nanowire on a Si substrate; bottom panel, cathodoluminescence images of the Au nanowire as a function of excitation wavelength. Adapted with permission.[188] (g) Electron energy-loss spectroscopy spectra measured from a 97 nm edge silver nanoprism, shown in the inset. Adapted with permission.[189] (h) High-angle annular dark field image obtained from the nanoprism of panel g.

synthesis in porous media.[167,169] Using synthesized NPs, periodic arrays and clusters of specific shapes can be produced by self-assembly on a substrate[7,170] or using DNA linking.[171−177] Another bottom-up approach involves the thermal evaporation of metal onto a substrate leading to the formation of NPs or nanoclusters.[178,179] However there is little control over the position, size, and shape of the particles.

Colloidal lithography[156,180] is a bottom-up process, which enables the fabrication of periodic arrays of metal NPs over a large area, such as the one shown in the top right panel of Figure 8. In this fabrication technique, polystyrene nanospheres deposited on a substrate self-assemble into an ordered array creating a mask. The mask can be made up of one or more layers of particles. Metal is then evaporated onto the mask, filling the holes between the spheres, and when it is removed, an array of metallic NPs remains on the substrate.

Top-down approaches differ from bottom-up methods because they do not involve chemical synthesis or self-assembly, and can be seen as an extension of microfabrication techniques. Deep ultraviolet projection lithography is a top-down approach that has been used to fabricate plasmonic waveguides.[181] However in order to obtain metallic structures with dimensions on the order of 80 nm or less, processes that are not diffraction-limited are necessary. Focused ion beam and electron beam lithography[157,182] are maskless sequential techniques that are widely used to fabricate nanostructures of different sizes or shapes very accurately on a substrate.[123,183] The bottom left panel of Figure 8 shows a dolmen-shaped NP obtained using this method. Due to the high cost and low throughput of these two methods, other processes such as soft[184] and nanoinprint[157] lithography have been developed. In these techniques, large numbers of complex nanostructures can be fabricated on a


dx.doi.org/10.1021/cr1002672 |*Chem. Rev.* 2011, 111, 3888–3912

substrate at low cost with high accuracy[157,182] using a mold made by electron beam lithography. The bottom right panel of Figure 8 shows an example of a silver grating fabricated using thermal nanoimprint lithography and shadow evaporation.[160]

There are many techniques available to study metallic nanostructures and their properties. We will focus on plasmon characterization methods, which can be divided into four categories according to the type of excitation and detection used,[185] as shown schematically in the center of Figure 9. In this figure, the rows relate to the excitation type and the columns to the type of detection.

LSPRs can be excited optically without the need for careful matching of the wavevector as in SPPs.[59] We consider first all optical characterization, which encompasses a wide range of different techniques, including the methods used to measure the data plotted in panel A of Figure 9. The position of the LSPR of an ensemble of NPs particles in solution,[190] in a matrix,[191,192] or on a planar substrate can easily be determined from a transmission spectrum assuming negligible inhomogeneous broadening due to size variation in the ensemble. Coupling optical spectroscopy and confocal microscopy enables the measurement of far-field spectra from single nanostructures on a substrate, as seen in the graph labeled a in Figure 9.[127] Using a dark field objective[158,193] on a confocal microscope or using the evanescent field created by total internal reflection from a prism[158,168,194] enables the measurement of the scattering spectrum from a single NP.

Due to the intrinsic ultrafast electronic dephasing, details about the local electric field distribution around metallic NPs cannot be extracted from the LSPR measured in the far-field.[79] The plasmon modes of metal nanostructures can be mapped by near-field optical processes such as leakage and fluorescent imaging[59,183,195,196] using a confocal microscope. Confocal microscopy can also be coupled with nonlinear optical processes, which have a higher power dependence on the electric field. This leads to improved sensitivity when probing the near-field of the particles. One such process is TPL,[107,197] where the luminescence is due to the interband transitions of gold. TPL therefore provides an all-optical probe-free approach for the study of the near-field around gold nanostructures. However methods based on a confocal microscope are diffraction-limited.

The amplitude and phase of the near-field around metallic nanostructures can be accurately studied using a near-field optical microscope (SNOM) and heterodyne detection technique. A range of probes have been used with SNOM including subwavelength apertures[198−201] and scatterers, such as atomic force microscope (AFM) tips,[119,186,202−206] carbon nanotubes,[207] and fluorescent molecules.[208] SNOM offers subdiffraction limit resolution[209] with the size of the aperture or tip of the scatterer limiting the lateral resolution.[210] However a SNOM probe can distort the results of the measurement due to its interaction with the sample.[204,210,211] Setting orthogonal polarizations for excitation and detection has been demonstrated as a means of decoupling the effects of the tip and sample as well as leading to background signal suppression.[210] This technique can be used in conjunction with optical spectroscopy and time-dependent measurements[212] as well as with nonlinear processes such as TPL and second and third harmonic generation.[158,202,213]

SEM can be used to image NPs as well as manipulate them, while TEM is another imaging tool available in plasmonics.[214] However, electron microscopes can also be used to excite and detect plasmon resonances in metal nanostructures.[215] The plasmons are excited by the focused electron probe due to the EM fields associated with fast moving charges. This means that electrons can also act as plasmon probes as a beam of charges passing close to or through an object yields information about its optical properties.

We consider now characterization techniques where both the excitation and detection of plasmons are due to electrons and not photons. Such methods yielded the data plotted in panel D of Figure 9. In scanning transmission electron microscope electron energy-loss spectroscopy (STEM-EELS) the LSPR spectrum can be measured, and the amplitude and spatial variation of surface plasmon resonances can be mapped.[111] However, the low-energy part of an EELS spectrum can be masked by the so-called zero-loss peak (ZLP), caused by electrons that are elastically scattered or have encountered too little loss. Electron energy filtering transmission electron microscopy (EEFTEM)[216] enables the suppression of the ZLP and faster spectral sampling but at the expense of the resolution. Plasmons have been mapped on single and coupled metallic NPs with high spatial and energy resolution using STEM-EELS and EEFTEM,[111,214,216−220] but the interpretation of a STEM-EELS spectrum is still open to debate.[221,222]

Having considered photon (Figure 9, panel A) and electron (Figure 9, panel D) excitation and detection in turn, there exist mixed methods, labeled B and C in Figure 9, where optically excited plasmons are detected via electrons and vice versa.

In photoemission electron microscopy (PEEM), a light source, such as a laser, is used to excite plasmons leading to the photoemission of electrons by metal nanoobjects, which are collected and analyzed. A PEEM experiment can be used to measure the LSPR spectrum as well as to image the near-field around metallic nanostructures, as shown in panel B of Figure 9. This experiment has subdiffraction limit resolution and does not require a probe to be placed in the near-field of the particle.[187,223] The dynamics of the plasmonic modes can also be temporally and spatially studied by coupling time-resolved TPL with a time-resolved PEEM detection system.[224,225] Photon-induced near-field electron microscopy (PINEM)[226] also has potential application in plasmonics, because it enables the near-field around NPs to be studied on a femtosecond time scale.

Lastly, the electron beam from a TEM used for excitation can be coupled with a light detection system. This technique, known as cathodoluminescence, offers the high excitation resolution of the electron beam as well as higher energy resolution in the optical regime than EELS.[227] Cathodoluminescence has been used for spectral measurements of LSPRs as well as to map plasmon modes in different geometries,[188,227,228] as illustrated in panel C of Figure 9.

## 4. EMITTERS CLOSE TO METAL NANOPARTICLES: INTERACTION WITH LOCALIZED SURFACE PLASMONS

Spontaneous emission occurs when an electron in an excited state of an atom, molecule, quantum dot, etc. decays to another state with lower energy. The frequency of the emitted light is given by

$$\hbar\omega = E_2 - E_1 \tag{22}$$

where $E_2$ is the energy of the upper level and $E_1$ is the energy of the lower level (see Figure 10). It is a well-known physical phenomenon studied in disciplines such as chemistry, physics,

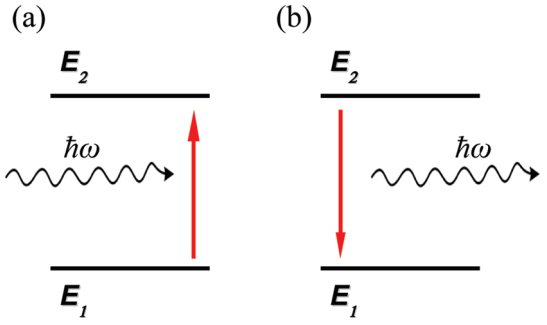


**Figure 10.** Sketch of the electronic transitions between two levels (of energies $E_1$ and $E_2$) of an emitter leading to absorption (a) and spontaneous emission (b) of photons.

and biology, with applications ranging from light-emitting diodes to fluorescent dyes, colorants, clinical assays, etc.

Spontaneous emission is a very intriguing physical process because it is one of the few macroscopic effects in nature that can only be described by means of a full quantum electrodynamic treatment. Note that quantum mechanics (in the first quantization framework) explicitly forbids spontaneous transitions. In fact, for an isolated atom in an excited state, that is, in an eigenstate of the Hamiltonian, there is no mechanism leading to electron decay, except for external perturbations acting on the system. This is because the two eigenstates (excited and ground levels) are orthogonal. We will later see that it is only possible to address the phenomenon of spontaneous emission in the context of a full quantum electrodynamic theory (second quantization). Surprisingly, the first quantitative description of spontaneous emission was proposed before the birth of quantum electrodynamics.[229,230] Einstein developed a phenomenological description of photon absorption and emission by atoms based on blackbody radiation, in which he distinguished spontaneous and stimulated emission channels and introduced transition rate coefficients.[229,230] In determining the Einstein coefficients, the only interaction of the emitter with the "external world" is through blackbody radiation. This led to the erroneous assumption that the emission properties are only determined by the emitter itself.

### 4.1. Spontaneous Emission Engineering: Purcell Effect

In 1946, Purcell[231] discovered that spontaneous emission not only is related to the emitter, but also depends on its environment. A very persuasive example is the case of an atom in a cavity with perfectly reflecting walls. If the dimensions of the cavity are smaller than half the wavelength of the atomic emission, no EM modes are supported by the system at a frequency, $\omega$, given by eq 22, and the atom will not decay. This means that we cannot consider an emitter and its environment as two separate entities because they interact and modify each other. We therefore need to consider the system comprising both emitter and environment as a whole.

As we mentioned above, the spontaneous emission of an isolated atom is due to an external perturbation and is forbidden in the first quantization picture. The situation is completely different if the EM field is also quantized (second quantization). In this case, the ground state, i.e., the absence of photons in the system, has an energy $E_{vac} = {}^1/_2\hbar\omega$, that is different from zero. Usually, this state is known as the zero-point energy and originates from random fluctuations of the electric field known as the vacuum field. This can interact with an isolated emitter in an excited state and can make it decay to a lower energy level. We can calculate the corresponding radiative transition rate using Fermi's golden rule[229]

$$\gamma = \frac{2\pi}{\hbar^2}|\langle f|\hat{\mu}\cdot\hat{\mathbf{E}}_{vac}|i\rangle|^2\rho(\omega) \tag{23}$$

where $\gamma$ is the transition decay rate from the initial (excited) state $|i\rangle$ to the final state $|f\rangle$, $\hat{\mu}$ and $\hat{\mathbf{E}}_{vac}$ are the electric dipole and vacuum-field operators evaluated at the emitter position, respectively, and $\rho(\omega)$ is the final photonic density of states.

Equation 23 enables us to consider the spontaneous emission of an excited state as the stimulated emission due to the zero-point fluctuations of the EM field. The density of final photonic states $\rho(\omega)$ is defined so that $\rho(E)dE$ gives the number of final states which fall into the energy range $E$ to $E+dE$, where $E=\hbar\omega$. One can calculate $\rho(\omega)$ in vacuum by considering the EM modes within a cube of volume $V$,[229] having

$$\rho(\omega) = V\rho_0 = V\frac{\omega^2}{\pi^2c^3} \tag{24}$$

Note that the arbitrary volume $V$ serves as a computational tool and that it will disappear in the final result. The magnitude $\rho_0$ is the local density of states (LDOS) for vacuum, that is, the number of final states (modes) per unit volume with frequency $\omega$. On the other hand, the transition matrix element in eq 23, averaged over all the possible directions, yields

$$|\langle f|\hat{\mu}\cdot\hat{\mathbf{E}}_{vac}|i\rangle|^2 = \frac{1}{3}\mu_{if}{}^2E_{vac}{}^2 \tag{25}$$

$\mu_{if}{}^2$ being the square modulus of the electric dipole moment of the transition

$$\mu_{if} = -e\langle i|\mathbf{r}|f\rangle \tag{26}$$

where $e$ is the electron charge and $\mathbf{r}$ is the position operator. The vacuum electric field can be obtained by equating the EM energy in a volume $V$ with the zero point energy

$$\int \varepsilon_0 E_{vac}{}^2\, dV = \frac{\hbar\omega}{2} \tag{27}$$

which implies

$$E_{vac} = \sqrt{\frac{\hbar\omega}{2\varepsilon_0 V}} \tag{28}$$

Hence using eqs 23−25 and 28, we obtain the decay rate of an isolated emitter

$$\gamma_{free} = \frac{1}{\tau_{free}} = \frac{\mu_{if}{}^2\omega^3}{3\pi\varepsilon_0\hbar c^3} \tag{29}$$

where $\tau_{free}$ is the radiative lifetime. Remarkably eq 29 has exactly the same form of the classical expression for the radiative damping of an electric dipole in vacuum.[44,58,59,232−234]

### 4.2. Weak Coupling

The contribution of emitter and environment to the decay rate, $\gamma$, split into two terms in eq 23. The matrix element takes into account the quantum mechanical properties of the emitter, while the density of states, $\rho(\omega)$, reflects the influence of the environment. A similar situation occurs when the emitter is placed in a cavity and their interaction is said to be weak[43,232,235,236]

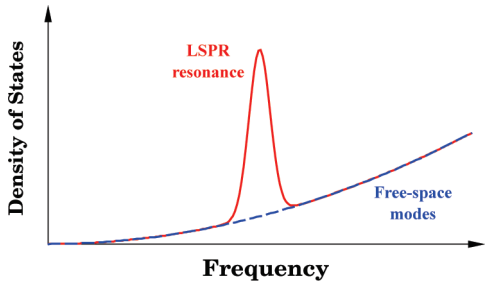


**Figure 11.** Schematic comparison between the density of photonic states in a plasmonic cavity (red solid line) and free-space (blue dashed line).

(we will give a formal definition of the weak interaction in section 4.3). Depending on the characteristics of the cavity, such as its dimensions, shape, and composition, only specific EM modes will be supported. This means that the cavity will only allow certain final states into which photons can decay. If, for instance, an emitter is placed close to a metal NP, the final density of states will have a peaked maximum at the plasmon resonance wavelength, as it provides a new and strong decay channel for the emitter (see Figure 11).

If we consider a cavity that supports only one mode of frequency, $\omega_c$, the density of states, $\rho(\omega)$, can be described by the Lorentzian function

$$\rho(\omega) = \frac{2}{\pi}\frac{\Delta\omega}{4(\omega-\omega_c)^2+\Delta\omega^2} \tag{30}$$

characterized by the quality factor, $Q = \omega_c/\Delta\omega$, of the cavity, where $\Delta\omega$ is the width of the LDOS maximum at $\omega = \omega_c$.[237]

If an emitter located in the cavity has an electronic transition at $\omega_0 = \omega_c$, the cavity is said to be tuned to the emission frequency, and the density of states at $\omega = \omega_0$ is

$$\rho(\omega_0) = \frac{2Q}{\pi\omega_0} \tag{31}$$

The fact that cavity and emitter are only weakly coupled enables us to relate the transition matrix elements of the system to those of the free emitter. Using eqs 25 and 28, we have

$$|\langle f|\hat{\mu}\cdot\hat{\mathbf{E}}|i\rangle|^2 = \beta^2\frac{|\mu_{if}|^2\hbar\omega}{2\varepsilon_0 V} \tag{32}$$

where $V$ is the cavity volume and $\beta$ is a factor that takes into account the dipole moment orientation

$$\beta = \frac{|\mu\cdot\mathbf{E}|}{|\mu||\mathbf{E}|} \tag{33}$$

Note that when it is randomly oriented, $\beta^2 = {}^1/_3$.

Using eqs 25 and 31, we can also calculate the decay rate of an emitter placed within a plasmonic cavity:

$$\gamma_{cav} = \beta^2\frac{2|\mu_{if}|^2}{\varepsilon_0\hbar}\frac{Q}{V} \tag{34}$$

It is interesting to compare the decay rate of the emitter in the cavity to that in free space. For an emitter parallel to the field direction ($\beta^2 = 1$), we find

$$F_P = \frac{\gamma_{cav}}{\gamma_{free}} = \frac{\tau_{free}}{\tau_{cav}} = \frac{3}{4\pi^2}Q\left(\frac{\lambda^3}{n^3V}\right) \tag{35}$$

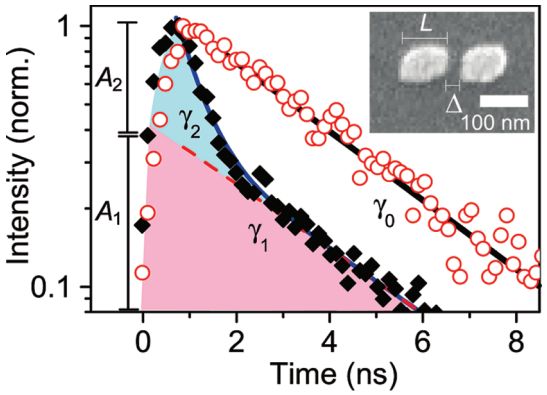


**Figure 12.** Normalized measurements of fluorescence decay rate for a dye near a resonant nanoantenna (black diamonds) and away from the nanoantenna (red circles), together with exponential decay fits (black and blue lines). Inset: SEM image of the resonant gold nanoantenna. Adapted with permission.[183]

where $F_P$ is known as the Purcell factor[23,237−239] and we have used $c/\omega = n(2\pi/\lambda)$, where $n$ is the cavity refractive index. $F_P$ describes how the decay rate of the emitter is modified by the presence of the cavity. If $F_P > 1$, the spontaneous decay rate is enhanced; otherwise the cavity inhibits the emission.

Equation 35 shows that $F_P$ is proportional to the quality factor, $Q$, of the plasmonic resonance and inversely proportional to the mode volume. As plasmonic structures concentrate EM fields into subwavelength volumes, they are suitable to manipulate the decay rate of emitters despite the fact that such structures do not have resonances with very high quality factors ($Q \approx 10-100$ or ${}^3/_4\pi^2 Q \approx 1-10$). However, the highly reduced mode volume of LSPRs enables a strong enhancement of the decay rate of emitters, given by the factor $\lambda^3/(n^3V)$ in eq 35.

An example of this effect is shown in Figure 12, where the radiative decay rate of dye molecules positioned close to gold nanoantennas is measured.[183] In this experiment, a pair of nanoantennas with dimensions of $90 \times 60 \times 20$ nm$^3$ are placed 20 nm apart (see inset of Figure 12). The dye used has a fluorescence decay time of 3.3 ns. The red circles in Figure 12 represent the fluorescence intensity (plotted on a log scale) versus time at the resonant frequency of the antennas at a position away from them. The black diamonds are the resonant fluorescence measurements taken just above the nanoantennas.

We can see that in the measurements without the nanoantennas (red circles), the intensity decay follows an exponential trend from which the decay rate can be extracted, $\gamma_0 \approx 0.3$ ns$^{-1}$. On the other hand, the presence of the nanoantennas modifies the fluorescence decay of the dye, leading to a multiexponential behavior (black diamonds). Two channels, leading to different decay rates, can be distinguished in this case. The slow decay channel corresponds to the molecules that are not coupled to the LSPR of the antennas and show a decay rate that is very similar to that observed in the absence of the metallic structures ($\gamma_1 \approx 0.3$ ns$^{-1}$). The fast decay rate is due to dye molecules located in the vicinity of the antennas, which are strongly coupled to the LSPRs excited in them. Remarkably the molecules affected by the presence of the nanoantennas decay ~5 times faster than the unperturbed ones ($\gamma_1 \approx 1.7$ ns$^{-1}$).

We have seen how plasmonic cavities enable the enhancement of the decay rate of an emitter placed in their vicinity. We have seen that a metal NP also acts as an optical antenna and enhances

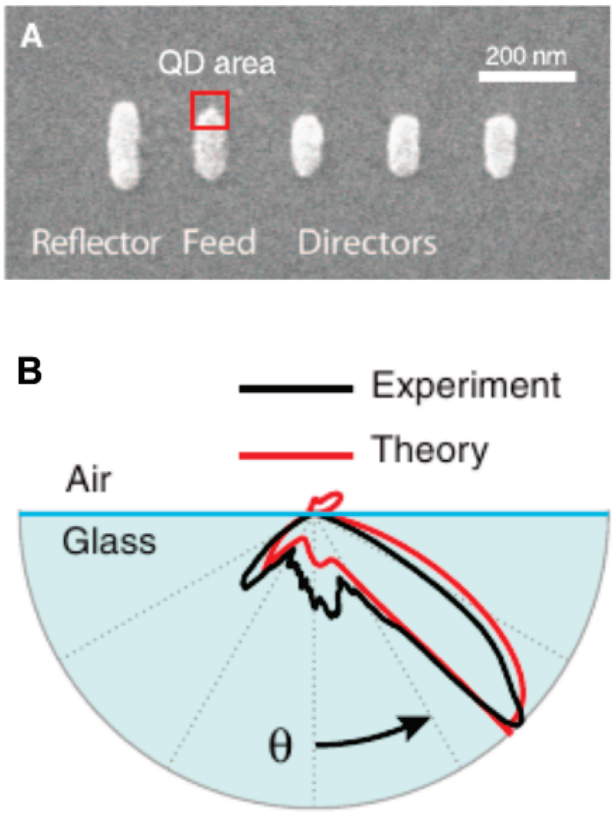


**Figure 13.** (a) SEM image of a five-element Yugi−Uda gold nanoantenna. A quantum dot is attached to one end of an arm, indicated with a red square. (b) Measurement (black line) and calculation (red line) of the radiation angular distribution for the structure. Adapted with permission.[244] Copyright 2010, American Association for the Advancement of Science.

the interaction between a dye molecule and the far-field in two ways. On the one hand, light can be concentrated from the far-field into the small subdiffraction regions,[8,44] where the emitter is positioned. On the other hand, plasmonic nanoantennas can enhance the outcoupling of radiation into the far-field.[8,44,87]

When an emitter is excited, its emission is not directional, meaning that its experimental detection involves large solid angles. Controlling and modifying the far-field of an emitter is an important issue in plasmonics, and it is particularly interesting to obtain directional beaming effects. The alteration of the angular pattern by means of nanoantennas has been demonstrated,[240] and Yagi−Uda antennas have been proposed to achieve high directionality through plasmonics.[241−243] These antennas are very common in the microwave regime and consist of arrays of coupled dipoles that drive the emission in a particular direction.

A quantum dot carefully positioned near a Yagi−Uda nanoantenna emits in the direction where the geometry leads to constructive interference. Only recently, Yagi-Uda nanoantennas have been used to verify this experimentally.[244] In this experiment, a quantum dot was positioned close to an arm of the antenna (see Figure 13a). By near-field coupling, the quantum dot excites the nanoantenna and the interference of the emission from each arm causes a directional angular radiation pattern, as shown in Figure 13b.

### 4.3. Strong Coupling

The quality factor, $Q$, of a cavity mode is linked to the time, $\tau_{cav} = 1/\gamma_{cav}$, that a photon spends in the cavity or, in the case of a plasmonic resonance, to the lifetime of the LSPR. This provides us with a strategy to quantify the strength of the interaction between the cavity and the emitter. If the lifetime of the LSPR is very short compared with the inverse of the spontaneous decay rate of the isolated emitter, we are in the limit of weak coupling. In this case, resonant photons are retained for a short time and interact very little with the emitter. A different scenario occurs when the lifetime of the plasmonic resonance is significantly longer than the spontaneous emission lifetime in free space.

In order to describe the strong interaction between cavity and emitter, we have to introduce their interaction probability. Strong and weak regimes of interaction can be distinguished on the basis of the atom-field coupling constant, $\kappa$,[59,237] which is defined as the interaction energy,

$$\hbar\kappa = |\mu_{if} \cdot \mathbf{E}_{vac}| \tag{36}$$

Using eq 28, we obtain

$$\kappa = \frac{\mu_{if}}{\hbar}\sqrt{\frac{\hbar\omega}{2\varepsilon_0 V}} \tag{37}$$

Weak coupling satisfies the condition $\kappa \ll \gamma_{cav}$. In this limit regime, the effect of the vacuum field on the emitter can be considered as a perturbation, and as we have seen previously, the cavity and emitter can be treated as two separate entities.

Strong coupling satisfies the condition $\kappa \gg \gamma_{cav}$. In this regime, photons remain in the cavity for a long time and are absorbed and re-emitted multiple times before being radiated out of the structure. This leads to a strong coupling between cavity and emitter, which must be considered as a unique system instead of two separate entities. Importantly, an accurate description of such a system can only be obtained through a full quantum electrodynamics treatment.

Equation 37 shows the benefit of using the small volumes of LSPR in the strong coupling regime. The strong coupling between single emitters and the LSPRs of metallic nanostructures represents an exciting frontier in plasmonics, in particular when considering its exploitation for quantum optics applications. Although it has been demonstrated that subwavelength confinement of guided plasmon modes in nanowires leads to a strong coupling between these EM modes and nearby emitters in the optical domain,[245−247] similar effects for LSPRs in metal NPs have not yet been shown.

## 5. NANOPARTICLE APPLICATIONS

Thus far, we have described how metal NPs can strongly interact with light and have shown that they can behave as receiving antennas by absorbing and concentrating incident light into a subdiffraction limited volume. NPs can also efficiently couple out stored energy, acting now as emitting antennas. These characteristics could lead to their use in the enhancement and manipulation of light interaction with emitters, with applications in various fields, such as SEF,[19−29,148,248,249] SERS,[18,30−42,248,250−252] plasmonic solar cells,[5,6,253−261] nanomedicine,[33,39,47−55] and sensing.[18,25,33,50,262] In this section, we very briefly outline some of the applications that are currently attracting much attention.

### 5.1. Surface-Enhanced Fluorescence

We have seen that the ability of metal nanostructures to concentrate light into small volumes enables the enhancement of

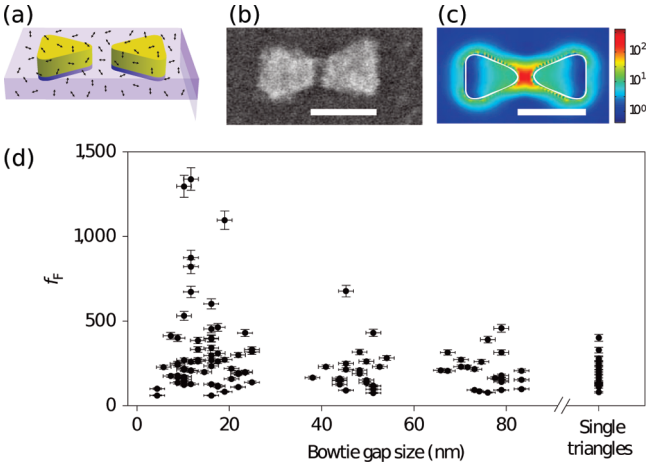


**Figure 14.** (a) Schematic representation of molecules randomly placed around a gold bowtie antenna on a transparent substrate. (b) SEM image of a gold bowtie antenna. Scale bar = 100 nm. (c) Calculation of the local electric field intensity enhancement. (d) Enhancement factor, $f_E$, from several nanoantennas as function of the gap size. Adapted with permission.[28] Copyright 2009, Nature Publishing Group.

the LDOS and thereby the decay rate of an emitter. However, when light is concentrated into subdiffraction volumes, another effect becomes relevant as well. The electric field in these small volumes becomes very intense, leading to the formation of hot spots[59,87] where the intensity of the incident field can easily be enhanced by a factor of $10^3$. Thus, placing a molecule in a hot spot also improves the efficiency of the optical excitation process.

For example, if we consider a dye molecule, the fluorescence enhancement, $f_F$, of the detected signal

$$f_F = \frac{\eta}{\eta_0}\frac{|\mu_{if}\cdot\mathbf{E}_{loc}|^2}{|\mu_{if}\cdot\mathbf{E}_0|^2} \qquad (38)$$

depends on both the incident, $\mathbf{E}_0$, and local electric field at the molecule position, $\mathbf{E}_{loc}$, as well as on the quantum efficiency of the molecule[21,20] close to, $\eta$, and far from, $\eta_0$, the nanostructure.

The quantum efficiency is defined as the ratio between the radiative decay rate, $\gamma_r$, and the total decay rate of the molecule, $\gamma$, given by the sum of the radiative and nonradiative decay rates,

$$\eta = \frac{\gamma_r}{\gamma} = \frac{\gamma_r}{\gamma_r + \gamma_{nr}} \qquad (39)$$

The nonradiative decay rate, $\gamma_{nr}$, reflects the absorption in the metal nanostructure and other intrinsic losses.

In a hot spot, the local field, $\mathbf{E}_{loc}$, is very large compared with the incident field, and from eq 38, we can anticipate that the fluorescence will be strongly enhanced. However, the highest $f_F$ is obtained only (see eq 38) when both the quantum efficiency $(\eta/\eta_0)$ and the local EM field are amplified.

A clear example of this effect has been recently shown by Kinkhabwala et al.[28] They have measured $f_F$ (see Figure 14d), for molecules placed in the gap of a gold bowtie antenna (see Figure 14a−c), obtaining a 1340-fold intensification of the emission. The dimensions of the gold triangles forming the antenna are about 100 nm, with a gap that is varied from 15 to 80 nm. The antennas were covered with a relatively inefficient dye ($\eta_0 \approx 2.5\%$), and the enhancement was high enough to

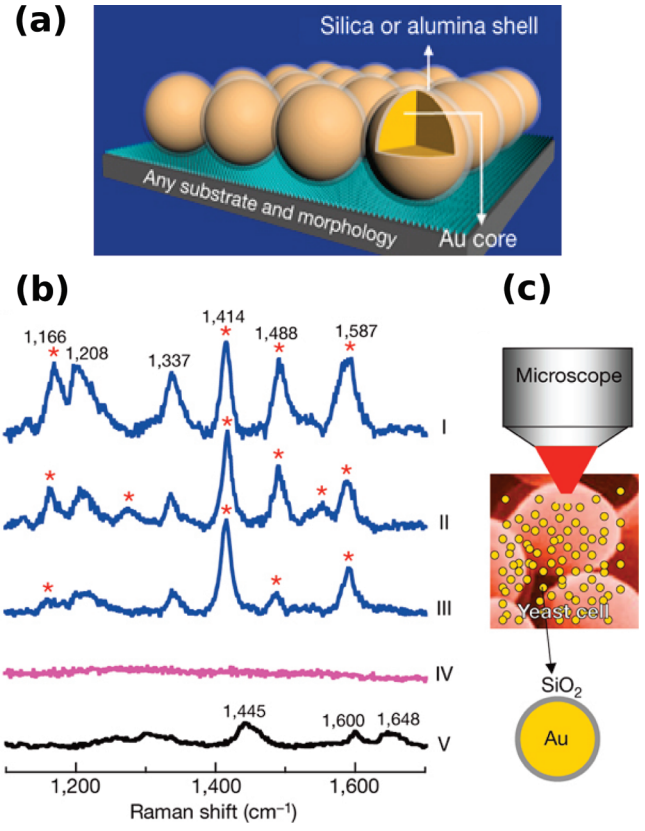


**Figure 15.** (a) Representation of an array of gold NPs covered with a ultrathin layer of silica or alumina. (b) Shell-isolated NP-enhanced Raman spectra obtained from different hot spots (curves I, II, and III) on the wall of a yeast cell incubated with $Au/SiO_2$ NPs. Curve IV is the spectrum obtained for bare NPs and curve V is a normal Raman spectrum for yeast cells. The peaks marked with red asterisks are closely related to mannoprotein. Adapted with permission.[267] Copyright 2010, Nature Publishing Group.

detect the contribution of single molecules. This was achieved by examining the time dependence of the fluorescence signal. By detection of a reduction of the signal due to irreversible photobleaching, it was possible to measure single-molecule contribution to the total fluorescence. The results shown in Figure 14d were obtained as a function of the bowtie gap size, showing a stronger enhancement for narrower gaps.

Fluorescence experiments usually suffer from two limitations. The first is diffraction-limited spatial resolution, constrained to about half the wavelength of the incident light. The second is limited brightness because there are only a small number of molecules close to the area being probed. Both these drawbacks can be overcome by making use of the excitation of localized surface plasmons in metal NPs.[28]

Importantly, the quantum efficiency and the near-field enhancement, which contribute to the fluorescence amplification, are evaluated at two different frequencies in eq 38. The electric field factor, $(|\mu_{if}\cdot\mathbf{E}_{loc}|^2/|\mu_{if}\cdot\mathbf{E}_0|^2)$, is calculated at the incident frequency that excites the LSPR (the absorption wavelength of the emitter), while the quantum efficiency enhancement, $(\eta/\eta_0)$, is calculated at the emission frequency. In order to maximize the fluorescence enhancement, it is important to design nanostructures that have plasmonic resonances whose frequencies


dx.doi.org/10.1021/cr1002672 |Chem. Rev. 2011, 111, 3888–3912

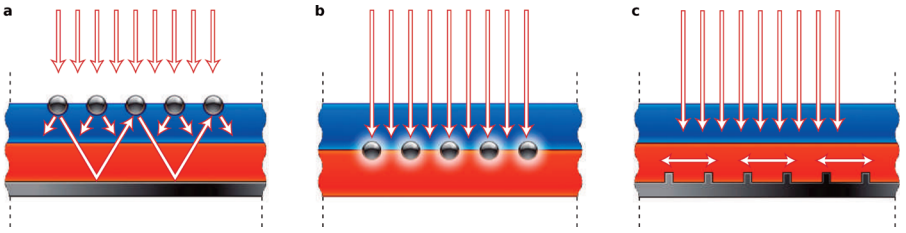


**Figure 16.** Schematic representation of different approaches to solar cells by means of plasmonic NP excitation: (a) light is trapped due to NP scattering; (b) light excites local surface plasmon polaritons, which enhance the absorption; (c) light is coupled to a guided mode. Adapted with permission.[6] Copyright 2010, Nature Publishing Group.

coincide with the absorption and emission spectral windows of the emitter, leading to a 2-fold effect.[117]

### 5.2. Surface-Enhanced Raman Scattering

A field that benefits greatly from the excitation of plasmons in metals is SERS spectroscopy. The SERS effect results from the enhancement of the Raman emission of molecules adsorbed onto rough metal surfaces, metal colloids, or metal NPs[263−265] and is due to two main effects, known as the chemical and the EM mechanisms. The chemical mechanism is linked to the formation of charge-transfer complexes, and the EM mechanism relates to the excitation of surface plasmons.[263,264] In the case of the EM mechanism, the SERS enhancement factor

$$G_{SERS} = \sigma(\omega)\sigma(\omega_R) \quad (40)$$

depends on the local electric field enhancement, $\sigma = |\mathbf{E}_{loc}|^2/|\mathbf{E}_{inc}|^2$, at the pump frequency, $\omega$, and at the Raman-shifted frequency, $\omega_R$.

When the Raman shift is small compared with $\omega$, the SERS enhancement factor of eq 40 has a fourth power dependence on the local electric field, that is, $G_{SERS} \approx |\mathbf{E}_{loc}|^4/|\mathbf{E}_{inc}|^4$. For this reason, typical enhancement factors obtained are $\sim 10^6$, and at best, it is possible to obtain factors as large as $\sim 10^{10}-10^{12}$. Such enhancement enables the detection of single molecules,[45,46,266] despite the fact that the Raman emission from isolated molecules is very low. In fact, SERS may be the most sensitive analytical technique.[265] Due to the high sensitivity of SERS, small differences in metal surface roughness or molecule position between samples limit the reproducibility of experimental results. Therefore, there is now an interest in using metal NP arrays, which can be accurately be fabricated, as SERS substrates.

A very interesting application of SERS has recently been reported by Li et al.[267] They propose a new spectroscopy technique in which the Raman signal amplification is provided by gold NPs with an ultrathin silica or alumina shell (see Figure 15a). Such NPs can be spread as a monolayer over the surface to be probed. The ultrathin layer covering the metal NPs keeps them from agglomerating and separates the NPs from direct contact with the material to be probed. It is the very small gap (~2 nm) between the NPs that leads to the strong electric field enhancements and associated high-quality Raman spectra. The authors call this new technique shell-isolated NP-enhanced Raman spectroscopy (SHINERS).

The Raman spectra of yeast cells (curves I−III) plotted in Figure 15b were measured at different locations of the same sample using SHINERS. These spectra are very different from the normal Raman spectra (curve V) of yeast cells, but similar to the SERS spectra of mannoprotein,[268] which is considered to be the main component of the yeast cell wall. The yeast cell walls are

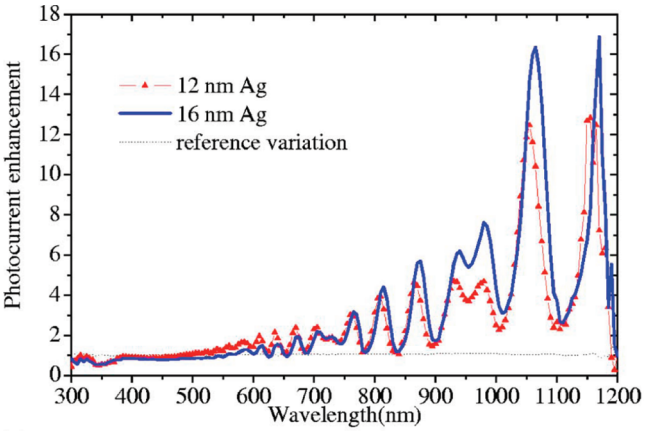


**Figure 17.** Photocurrent enhancement from a SOI solar cell improved with silver NPs with different dimensions. Adapted with permission.[253] Copyright 2007, American Institute of Physics.

of considerable interest due to their sensitivity to the different biological functions of the cell.

Another remarkable example of an application based on the SERS effect was given by Ward et al.,[269] who made electromigrated nanoscale gaps for SERS. They showed a method for producing planar electrodes with very small gaps of around 5 nm, where it was possible to detect Raman emission coming from a small number of molecules. The advantage of these nanojunctions is that they can be mass produced, allowing large SERS enhancements over a broad band of illumination.

### 5.3. Plasmonic Solar Cells

Photovoltaic light conversion is an important green technology that can be a viable solution to the energy and pollution problems worldwide. However, photovoltaics still cannot compete with fossil-fuel technologies. Current photovoltaic technology is mostly based on crystalline silicon wafers with thicknesses around 100−300 $\mu$m.[6] The production of such wafers represents most of the cost of a solar cell,[6] and the conversion efficiency of such cells needs to be improved. This situation can only change by reducing the amount of silicon being used, leading to a decrease in the price of the solar cell, while at the same time increasing their conversion efficiency.

Plasmonic photovoltaics is one of the most exciting fields in nanophotonics at the moment.[5,6,253−261] Standard solar cells are combined with metallic nanostructures, which concentrate and guide light at the nanoscale, leading to a reduction of the semiconductor thickness required, as well as enhancing the absorption of the incident light.[6]

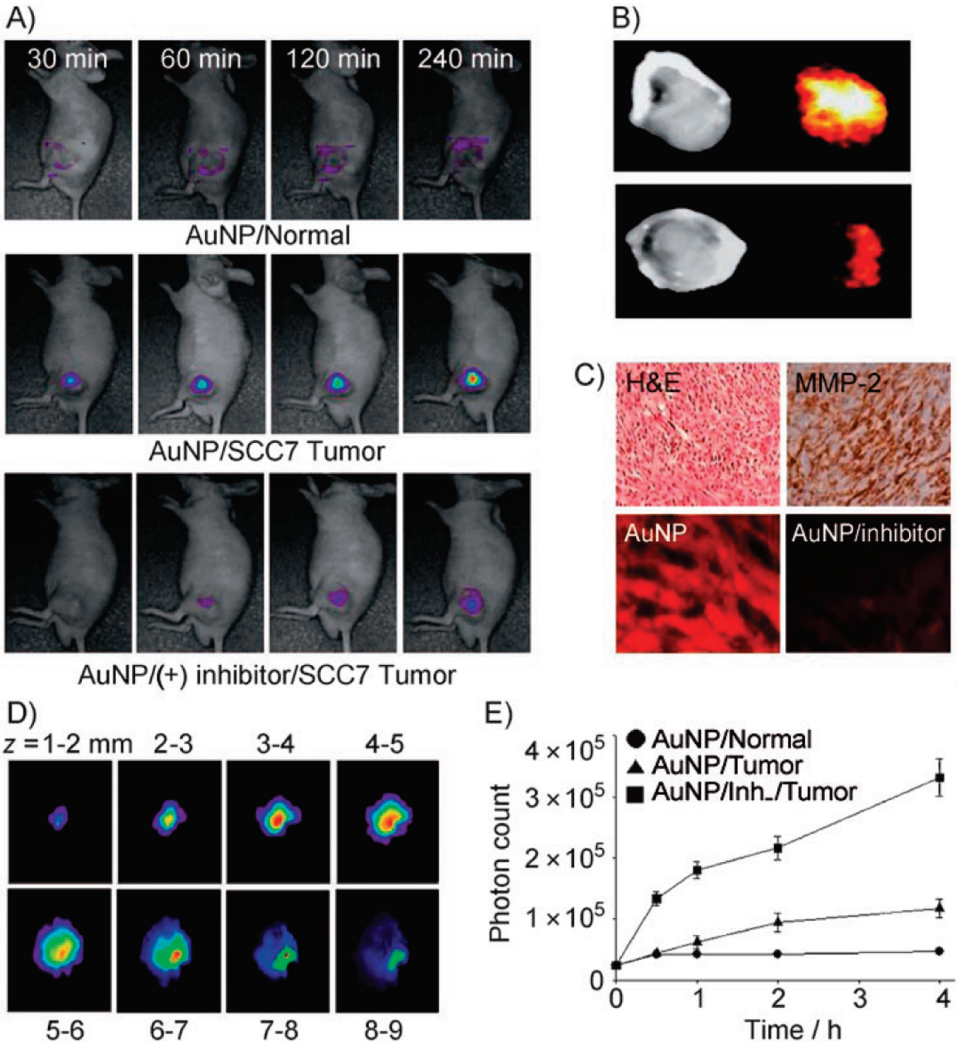


**Figure 18.** (A) Near-infrared fluorescence tomographic images of normal and subcutaneous tumor-bearing mice after injection of a gold NP probe with and without inhibitor (blue, low intensity; red, high intensity). (B) Near infrared fluorescence images of excised gold NP-probe-treated tumors with and without inhibitor. (C) Upper row, immunohistology results for tumors with different inhibitors; lower row, near-infrared fluorescence microscopy images of tumors containing gold NP probes without and with inhibitor. (D) 2D slices of the image from panel A reconstructed in the *z* direction (blue, low concentration; red, high concentration). (E) Quantitative image analysis performed by counting the total number of photons in the tumors as a function of time. Adapted with permission.[281] Copyright 2008, Wiley-VCH Verlag GmbH & Co. KGaA.

There are three main configurations being studied (Figure 16). The first approach makes use of the light scattering properties of metal NPs. The idea is to create a situation where incident sunlight is trapped in the semiconductor due to scattering effects (see Figure 16a). In the second strategy, incident light excites localized surface plasmons, which concentrate it. This leads to the creation of regions where the electric field is very intense (see Figure 16b). In this configuration, the NPs are close to the semiconductor, and because the absorption in the semiconductor is proportional to the local electric field intensity, the absorption enhancement takes place where the electric field is amplified. In the third case, NPs couple the incident light into a guided mode in the semiconductor, which propagates until it is completely absorbed by the active medium (see Figure 16c).

The idea of using plasmonic resonances to manipulate light and improve the absorption in semiconductor materials dates back to 1998, when Stuart and Hall[270] showed that silver nanoparticles deposited onto silicon leads to a 20-fold enhancement of photocurrent at 800 nm. More recently, it has been demonstrated that plasmonic structures can amplify photoabsorption of the photocurrent generated in the cell in several different physical situations. There are interesting examples reported on quantum well structures,[271] c-Si and GaAs solar cells,[272,273] ultrathin-film organic cells,[274] organic bulk heterojunctions cells,[275] and silicon-on-insulator (SOI) devices[253] Figure 17 illustrates the occurrence of photocurrent enhancement in plasmonic solar cells. The system consists of silver NPs deposited on a 1.25 $\mu$m thick SOI substrate, with a 30 nm height intermediate oxide layer.[253] In this experiment, metal NPs that have LSPRs in the visible and near-infrared scatter light leading to the formation of guided modes, which increase the amount of light trapped in the silicon film. The resulting photocurrent generated was normalized to that generated by the bare SOI structure and is shown in Figure 17. The photocurrent enhancement, which corresponds to a 33% increase in the total current of


dx.doi.org/10.1021/cr1002672 |*Chem. Rev.* 2011, 111, 3888–3912

the device, is due to different NP depositions and is particularly pronounced at longer wavelengths, where the silicon is less absorbing.

In recent years, there have been experimental advances in plasmonic photovoltaics. These have been accompanied by increasing efforts devoted to quantify theoretically the photoabsorption limit in plasmonic photovoltaics. Initial work was carried out by Yablonovitch,[276] who showed that the maximum absorption enhancement in an active medium (normalized to the incident EM energy) cannot exceed $2n^2$, where $n$ is the refractive index. This is the so-called ergodic limit,[276] which was calculated in the framework of statistical ray optics considering randomly textured surfaces. These assumptions are no longer valid in plasmonic structures, which are subwavelength and are not randomly textured. This means that the statistical approach based on ray optics is not suitable to describe light scattering from a plasmonic solar cell.

Researchers are currently studying the absorption enhancement limit in these new structures, and recent works have shown that the ergodic limit can be exceeded.[277,278] However, more accurate analyses are needed in order to find the fundamental absorption limit in nanophotonics.

### 5.4. Nanomedicine

Although gold NPs have been used in biomedical applications for almost 40 years,[279] the range of applications has increased recently due to advances in biotechnology as well as NP synthesis and conjugation. The use of nonspherical metal particles[47,49,280] for biomedical applications allows the tuning of LSPR to the medical window (650−900 nm), where light penetrates much deeper into living tissue, and the scattering to absorption ratio can be tuned.[47]

The imaging of biological samples and the detection of diseases such as cancer require biomarkers and contrast agents. Traditionally, these were based on photoabsorbing and fluorescent dyes, and more recently, quantum dots have been also proposed. However, both are prone to photobleaching. Therefore, there is an interest in exploiting the large scattering cross sections associated with LSPRs. Moreover, unlike dyes or quantum dots, they do not photobleach and can be nontoxic.[281,282] An example of *In Vivo* gold NP imaging can be seen in Figure 18.[281] Gold particles are also being investigated for use in drug and gene delivery;[282] application relies on both their biostability and optical properties. Due to their biostability, gold particles have also been proposed as contrast agents for magnetic resonance imaging.[283]

The absorptive properties of metal NPs are also promising for medical imaging. Small spherical NPs with diameter ≤20 nm or optimized nonspherical geometries mostly absorb light. This leads to a local increase in the temperature of the host as the NP cools, which can be used to image the particle. Photothermal imaging relies on the change of the refractive index of the host with increasing temperature, while photoacoustic imaging monitors the thermal expansion of the host.

The main interest in the absorptive properties of metal NPs lies in exploitation of their resistive heating for medical treatment. A laser can be used to ablate tumors in the presence of photoabsorbers. Using gold particles as the photoabsorbers maximizes the light absorption due to the large cross section associated with their LSPR, which leads to a reduction of the intensity of radiation required.[52,284,285] The idea is to introduce

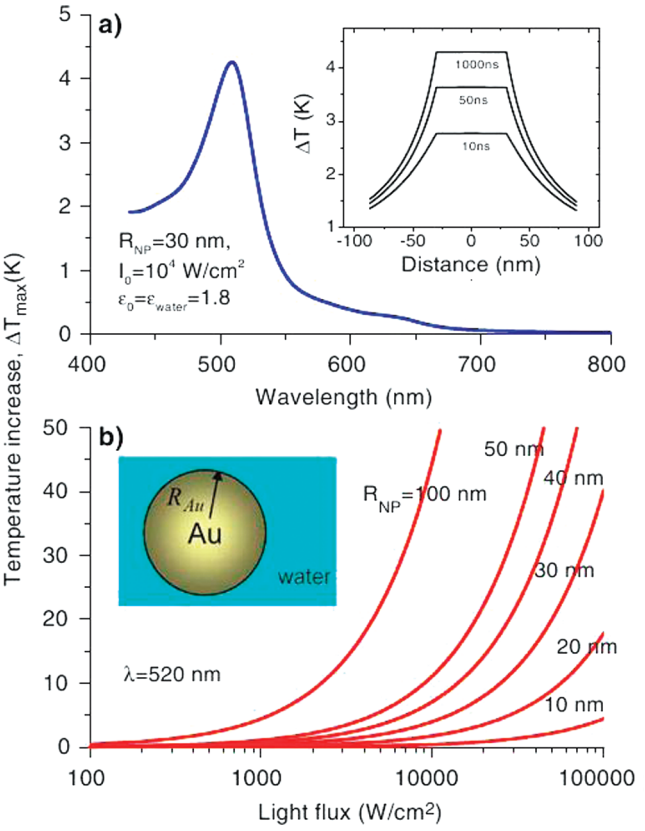


**Figure 19.** Calculated temperature variation for gold spherical nanoparticles in water as a function of the incident wavelength (a) and incident power (b) for different radii. Inset of panel a shows the time dependence of the temperature increase within the nanoparticle. The calculations in panel b are performed at the LSPR frequency. Adapted with permission.[286] Copyright 2006, Springer.

specifically designed metal NPs into tumor cells, with dimensions allowing the excitation of LSPRs at wavelengths where the human body is almost transparent. The excitation of plasmonic resonances causes a temperature increase in the particles that can be lethal for tumors. It is possible to show that the absorbed power density in an arbitrary structure, as function of the vector position $\mathbf{r}$, is

$$Q(\mathbf{r}) = \frac{\omega}{2\pi} \mathrm{Im}[\varepsilon(\mathbf{r},\omega)]|\mathbf{E}(\mathbf{r},\omega)|^2 \qquad (41)$$

which is proportional to the imaginary part of the dielectric constant, $\varepsilon(\mathbf{r},\omega)$, and the local electric field intensity, $|\mathbf{E}(\mathbf{r},\omega)|^2$. The absorbed energy, $Q(\mathbf{r})$, represents the heat source due to light dissipation in the metal particle and is obtained by solving Maxwell's equations. Once $Q(\mathbf{r})$ is known, the temperature distribution inside and outside the NP can be calculated using the heat transfer equation

$$\rho(\mathbf{r})c(\mathbf{r})\frac{\partial T(\mathbf{r},t)}{\partial t} = \nabla k(r)\nabla T(\mathbf{r},t) + Q(\mathbf{r}) \qquad (42)$$

where $\rho(r)$, $c(r)$, and $k(r)$ are the mass density, specific heat, and thermal conductivity, respectively, and $T(\mathbf{r},t)$ stands for the time-dependent local temperature. The solution of eq 42 has a transient state, and after a characteristic time, $\tau$, it reaches its steady state.[54,286−288]


dx.doi.org/10.1021/cr1002672 |*Chem. Rev.* 2011, 111, 3888–3912

Thermal processes in metals are fast, which means that a steady state is rapidly reached for typical powers and metal NP dimensions used in nanomedicine.[52,284,285] Therefore a simplified time-independent heat equation can be considered instead of eq 42

$$\nabla[k(\mathbf{r})\nabla(T(\mathbf{r}))] = -Q(\mathbf{r}) \quad (43)$$

Because heat flow is fast in the metal, the nanostructure temperature is nearly uniform for small particles.[54,289,290] The temperature distribution inside and outside spherical gold NPs in water is shown in Figure 19 as a function of the wavelength (panel a) and the incident power (panel b). The inset in Figure 19a shows the temperature increase with time. Note that the maximum temperature in panel a occurs at $\lambda$ = 520 nm for a gold sphere of 30 nm radius. This peak corresponds to the excitation of a LSPR in the system. In Figure 19b, we can see that larger temperature increases are obtained for bigger spheres, as expected, because the absorbed energy is proportional to the NP volume (assuming a constant energy distribution within it).

## 6. CONCLUSIONS

In this paper, we have reviewed fundamental concepts, recent advances, and applications concerning the interaction of nanoantennas with light and emitters, such as fluorescent molecules and quantum dots.

It has been shown that nanoantennas designed to interact strongly with radiation in the optical regime can be used to manipulate light on the nanoscale through the excitation of plasmonic modes. Notions such as localized surface plasmon resonances have been explained in a tutorial-like manner introducing electromagnetic cross sections, plasmon hybridization, plasmonics dark modes, Fano resonances, and coherent coupling in nanoparticle arrays. We have also reviewed the current state of the art in nanofabrication and characterization techniques available for nanoplasmonics.

Nanoantennas can drastically modify the emission properties of quantum dots or fluorescent molecules placed in their vicinity. In this context, they act as plasmonic cavities, which enable the control and enhancement of the radiative properties of light emitters. We have described the fundamental physics behind this intrinsically quantum effect, and depending on the intensity of the emitter−nanoantenna interaction, two different regimes have been identified and discussed. We have shown that metal nanoparticles do not only enable the efficient extraction of electromagnetic energy from poor emitters but also allow the tailoring of the radiation pattern emerging from them.

The remarkable electric field enhancement and confinement that nanoantennas provide have relevant fundamental and technological implications in areas such as surface-enhanced fluorescence, surface-enhanced Raman scattering spectroscopy, plasmonic solar cells, and nanomedicine. The implementation of plasmonic concepts in these different areas has been described, and some of the prospects that nanoantenna capabilities open up in research areas such as nonlinear optics and quantum photonics have been also briefly discussed.

In order to obtain plasmonic nanostructures with high quality factor resonances and strong light concentration, small gaps and carefully designed structures need to be fabricated with nanometer scale resolution in a reproducible manner. This remains a challenge when using current fabrication technologies. Once these constraints have been overcome, it will be possible to take advantage of all the benefits offered by nanoplasmonics.

## AUTHOR INFORMATION

### Corresponding Author

*E-mail: v.giannini@imperial.ac.uk.

## BIOGRAPHIES

Vincenzo Giannini studied physics at the University of Pisa (Italy). He achieved his Ph.D. in theoretical condensed matter physics at Universidad Autónoma de Madrid (Spain) working on the strong interaction of light with metal nanoparticles and the excitation of localized surface plasmons. He then had a joint postdoctoral position at the FOM Institute for Atomic and Molecular Physics (AMOLF) in Amsterdam and at Philips Research in Eindhoven. He is currently a Marie Curie fellow in the physics department at Imperial College London where his research interests include theoretical plasmonics and nano-optics.

Antonio I. Fernández-Domínguez received M.S. and Ph.D. (Hons) degrees in condensed matter physics from the Universidad Autónoma de Madrid, Spain, in 2004 and 2009, respectively. Since then, he has been working in the field of theoretical plasmonics and metamaterials as a postdoctoral researcher and a Marie Curie fellow in the Department of Physics, Imperial College London, U.K.

Susannah C. Heck received a B.Sc. (Hons) degree in physics from University College Cork, Ireland, in 2005. In 2009, she was awarded a Ph.D. from the Tyndall National Institute, University College Cork, Ireland, for her work on gain and loss mechanisms in semiconductor quantum dot and dash lasers and optical amplifiers. She then held a postdoctoral position at Imperial College London, U.K., in the area of plasmonics before joining the R&D team at Oclaro in February 2011.

Stefan Maier is Professor of Nanophotonics in the Physics Department and a Co-Director of the Centre for Plasmonics & Metamaterials at Imperial College London. In 2009, he also became Visiting Professor at A*STAR Institute for Materials Research & Engineering (IMRE), Singapore. Research in his group comprises fundamental light/matter interactions on the nanoscale as well as applied design of metamaterials, now aspiring to integrated biological sensors. Stefan is a Fellow of the Optical Society of America. His contributions to nanostructured optical metallic waveguides and high-confinement plasmon waveguiding in the terahertz regime found much acclaim in the surging field of plasmonics, earning him the Paterson medal and the Sackler Prize in Physics in 2010.

## ACKNOWLEDGMENT

This work was sponsored by the Engineering and Physical Sciences Research Council (EPSRC). V.G. and A.I.F.-D. acknowledge funding from the EU through the Marie Curie IEF program. The authors thank Nicholas Hylton for helpful comments during the preparation of this manuscript.

## REFERENCES

(1) Mühlschlegel, P.; Eisler, H.-J.; Martin, O. J. F.; Hecht, B.; Pohl, D. W. *Science* **2005**, *308*, 1607.
(2) Murray, W.; Barnes, W. *Adv. Mater.* **2007**, *19*, 3771.
(3) Lal, S.; Link, S.; Halas, N. J. *Nat. Photonics* **2007**, *1*, 641.
(4) Dong, Z. C.; Zhang, X. L.; Gao, H. Y.; Luo, Y.; Zhang, C.; Chen, L. G.; Zhang, R.; Tao, X.; Zhang, Y.; Yang, J. L.; Hou, J. G. *Nat. Photonics* **2009**, *4*, 50.
(5) Schuller, J. A.; Barnard, E. S.; Cai, W.; Jun, Y. C.; White, J. S.; Brongersma, M. L. *Nat. Mater.* **2010**, *9*, 193.
(6) Atwater, H. A.; Polman, A. *Nat. Mater.* **2010**, *9*, 205.
(7) Fan, J. A.; Wu, C.; Bao, K.; Bao, J.; Bardhan, R.; Halas, N. J.; Manoharan, V. N.; Nordlander, P.; Shvets, G.; Capasso, F. *Science* **2010**, *328*, 1135.
(8) Giannini, V.; Fernández-Domínguez, A. I.; Sonnefraud, Y.; Roschuk, T.; Fernández-García, R.; Maier, S. A. *Small* **2010**, *6*, 2498.
(9) Faraday, M. *Philos. Trans. R. Soc. London* **1857**, *147*, 145.
(10) Rayleigh, L. *Philos. Mag.* **1871**, *107*, 274.
(11) Rayleigh, L. *Philos. Mag.* **1899**, *41*, 375.
(12) Mie, G. *Ann. Phys. (Leipzig)* **1908**, *25*, 377.
(13) Gans, R. *Ann. Phys. (Leipzig)* **1912**, *37*, 881.
(14) Fleischmann, M.; Hendra, P.; McQuillan, A. *Chem. Phys. Lett.* **1974**, *26*, 163.
(15) Jeanmaire, D.; Van Duyne, J. *Electroanal. Chem.* **1977**, *84*, 1.
(16) Albrecht, M. G.; Creighton, J. A. *J. Am. Chem. Soc.* **1977**, *99*, 5215.
(17) Nehl, C. L.; Liao, H.; Hafner, J. H. *Nano Lett.* **2006**, *6* (4), 683.
(18) Hrelescu, C.; Sau, T. K.; Rogach, A. L.; Jäckel, F.; Feldmann, J. *Appl. Phys. Lett.* **2009**, *94*, No. 153113.
(19) Lakowicz, J. *Anal. Biochem.* **2004**, *324*, 153.
(20) Kühn, S.; Håkanson, U.; Rogobete, L.; Sandoghdar, V. *Phys. Rev. Lett.* **2006**, *97*, 1.
(21) Anger, P.; Bharadwaj, P.; Novotny, L. *Phys. Rev. Lett.* **2006**, *96*, No. 113002.
(22) Zhang, J.; Lakowicz, J. R. *Opt. Express* **2007**, *15*, 2598.
(23) Mohammadi, A.; Sandoghdar, V.; Agio, M. *New. J. Phys.* **2008**, *10*, No. 105015.
(24) Zoriniants, G.; Barnes, W. L. *New. J. Phys.* **2008**, *10*, No. 105002.
(25) Zhang, J. Z.; Noguez, C. *Plasmonics* **2008**, *3*, 127.
(26) Park, Q.-H. *Contemp. Phys.* **2009**, *50*, 407.
(27) Pustovit, V.; Shahbazyan, T. *Phys. Rev. Lett.* **2009**, *102*, 1.
(28) Kinkhabwala, A.; Yu, Z.; Fan, S.; Avlasevich, Y.; Müllen, K.; Moerner, W. E. *Nat. Photonics* **2009**, *3*, 654.
(29) Lakowicz, J.; Fu, Y. *Laser Photonics Rev.* **2009**, *3*, 221.
(30) Zeman, E. J.; Schatz, G. C *J. Phys. Chem.* **1987**, *91*, 634.
(31) Xu, H.; Aizpurua, J.; Kall, M.; Apell, P. *Phys. Rev. E* **2000**, *62*, 4318.
(32) Le Ru, E. C.; Etchegoin, P. G.; Meyer, M. *J. Chem. Phys.* **2006**, *125*, No. 204701.
(33) Jain, P. K.; Huang, X.; El-Sayed, I. H.; El-Sayed, M. A. *Plasmonics* **2007**, *2*, 107.
(34) Etchegoin, P. G.; Le Ru, E. C. *Phys. Chem. Chem. Phys.* **2008**, *10*, 6079.
(35) Zhang, S.; Genov, D. A.; Wang, Y.; Liu, M.; Zhang, X. *Phys. Rev. Lett.* **2008**, *101*, No. 047401.
(36) Xie, J.; Zhang, Q.; Lee, J. Y.; Wang, D. I. *ACS Nano* **2008**, *2*, 2473.
(37) Spuch-Calvar, M.; Rodrguez-Lorenzo, L.; Morales, M. P.; Álvarez Puebla, R. A.; Liz-Marzán, L. M. *J. Phys. Chem. C* **2009**, *113*, 3373.
(38) Montgomery, J. M.; Imre, A.; Welp, U.; Vlasko-Vlasov, V.; Gray, S. K. *Opt. Express* **2009**, *17*, 8669.
(39) Bardhan, R.; Chen, W.; Perez-Torres, C.; Bartels, M.; Huschka, R. M.; Zhao, L. L.; Morosan, E.; Pautler, R. G.; Joshi, A.; Halas, N. J. *Adv. Funct. Mater.* **2009**, *19*, 3901.
(40) Fang, Y.; Wei, H.; Hao, F.; Nordlander, P.; Xu, H. *Nano Lett.* **2009**, *9*, 2049.

(41) Giannini, V.; Rodriguez-Oliveros, R.; Sánchez-Gil, J. A. *Plasmonics* **2010**, *5*, 99.
(42) Wustholz, K. L.; Henry, A.-I.; McMahon, J. M.; Freeman, R. G.; Valley, N.; Piotti, M. E.; Natan, M. J.; Schatz, G. C.; Duyne, R. P. V. *J. Am. Chem. Soc.* **2010**, *132*, 10903.
(43) Barnes, W. L. *J. Mod. Opt* **1998**, *45*, 661.
(44) Bharadwaj, P.; D., B; Novotny, L. *Adv. Opt. Photonics* **2009**, *1*, 438.
(45) Kneipp, K.; Wang, Y.; Kneipp, H.; Perlman, L. T.; Itzkan, I.; Dasari, R. R.; Feld, M. S. *Phys. Rev. Lett.* **1997**, *78*, 1667.
(46) Nie, S.; Emory, S. R. *Science* **1997**, *275*, 1102.
(47) Lee, K.-S.; El-Sayed, M. A. *J. Phys. Chem. B* **2005**, *109*, 20331.
(48) El-Sayed, I. H.; Huang, X.; El-Sayed, M. a. *Cancer Lett.* **2006**, *239*, 129.
(49) Skrabalak, S. E.; Chen, J.; Au, L.; Lu, X.; Li, X.; Xia, Y. *Adv. Mater.* **2007**, *19*, 3177.
(50) Kumar, S.; Harrison, N.; Richards-Kortum, R.; Sokolov, K. *Nano Lett.* **2007**, *7*, 1338.
(51) Mallidi, S.; Larson, T.; Aaron, J.; Sokolov, K.; Emelianov, S. *Opt. Express* **2007**, *15*, 6583.
(52) Lapotko, D. *Nanomedicine* **2009**, *4*, 253.
(53) Srivastava, S.; Santos, A.; Critchley, K.; Kim, K.-S.; Podsiadlo, P.; Sun, K.; Lee, J.; Xu, C.; Lilly, G. D.; Glotzer, S. C.; Kotov, N. A. *Science* **2010**, *327*, 1355.
(54) Baffou, G.; Quidant, R.; García de Abajo, F. J. *ACS Nano* **2010**, *4*, 709.
(55) Zhou, Y.; Wu, X.; Wang, T.; Ming, T.; Wang, P. N.; Zhou, L. W.; Chen, J. Y. *J. Microsc.* **2010**, *237*, 200.
(56) van de Hulst, H. C. *Light Scattering by Small Particles*; Dover Publication: New York, 1981.
(57) Bohren, C. F.; Huffman, D. R. *Absorption and Scattering of Light by Small Particles*, 3rd ed.; Wiley-VCH: Weinheim, Germany, 2004.
(58) Jackson, J. D. *Classical Electrodynamics*, 3rd ed.; John Wiley & Sons: New York, 1999.
(59) Novotny, L.; Hecht, B. *Principles of Nano-Optics*; Cambridge University Press: New York, 2006.
(60) Zhao, J.; Pinchuk, A. O.; McMahon, J. M.; Li, S.; Ausman, L. K.; Atkinson, A. L.; Schatz, G. C. *Acc. Chem. Res.* **2008**, *41*, 1710.
(61) Kelly, K. L.; Coronado, E.; Zhao, L. L.; Schatz, G. C. *J. Phys. Chem. B* **2003**, *107*, 668.
(62) Johnson, P. B.; Christy, R. W. *Phys. Rev. B* **1972**, *6*, 4370.
(63) Born, M.; Wolf, E. *Principles of Optics*; Cambridge University Press: Cambridge, U.K., 1999.
(64) Newton, R. G. *Am. J. Phys.* **1976**, *44*, 639.
(65) Palik, E. D. *Handbook of Optical Constants of Solids*; Academic Press: New York, 1985.
(66) Palik, E. D. *Handbook of optical constants of Solids II*; Academic Press: Boston, 1991.
(67) Weber, M. J. *Handbook of Optical Materials*; CRC: New York, 2003.
(68) Ordal, M. A.; Long, L. L.; Bell, R. J.; Bell, S. E.; Bell, R. R., Jr.; R. W. A.; Ward, C. A. *Appl. Opt.* **1983**, *22*, 1099.
(69) Rakic, A. D.; Djurisic, A. B.; Elazar, J. M.; Majewski, M. L. *Appl. Opt.* **1998**, *37*, 5271.
(70) Vial, A.; Grimault, A. S.; Macias, D.; Barchiesi, D.; de la Chapelle, M. L. *Phys. Rev. B* **2005**, *71*, No. 085416.
(71) Hao, F.; Nordlander, P. *Chem. Phys. Lett.* **2007**, *446*, 115.
(72) Rodrigo, S. G.; García-Vidal, F. J.; Martin-Moreno, L. *Phys. Rev. B* **2008**, *77*, No. 075401.
(73) Dasgupta, B. B.; Fuchs, R. *Phys. Rev. B* **1981**, *24*, 554.
(74) Fuchs, R.; Claro, F. *Phys. Rev. B* **1987**, *35*, 3722.
(75) García de Abajo, F. J. *J. Phys. Chem. C* **2008**, *112*, 17983.
(76) McMahon, J. M.; Gray, S. K.; Schatz, G. C. *Phys. Rev. Lett.* **2009**, *103*, No. 097403.
(77) Zuloaga, J.; Prodan, E.; Nordlander, P. *Nano Lett.* **2009**, *9*, 887.
(78) Genzel, L.; Martin, T. P.; Kreibig, U. *Z. Phys. B* **1975**, *21*, 339.
(79) Kreibig, U.; Vollmer, M. *Optical Properties of Metal Clusters*; Springer Series in Materials Science; Springer-Verlag: Berlin, 1995.
(80) Ritchie, R. H. *Phys. Rev.* **1957**, *106*, 874.
(81) Raether, H. *Surface Plasmons on Smooth and Rough Surfaces and on Gratings*; Springer Verlag: New York, 1988.
(82) Barnes, W. L.; Dereux, A.; Ebbesen, T. M. *Nature* **2003**, *424*, 824.
(83) Zayats, A. V.; Smolyaninov, I. I.; Maradudin, A. A. *Phys. Rep* **2005**, *408*, 131.
(84) Ozbay, E. *Science* **2006**, *311*, 189.
(85) Maier, S. A. *IEEE J. Sel. Top. Quantum Electron.* **2006**, *12*, 1214.
(86) Ebbesen, T. M.; Genet, C.; Bozhevolnyi, S. I. *Phys. Today* **2008**, *61*, 44.
(87) Maier, S. A. *Plasmonics: Fundamentals and Applications*; Springer: New York, 2007.
(88) Yee, K. S. *IEEE Trans. Antennas Propag.* **1966**, *14*, 302.
(89) Taflove, A. *IEEE Trans. Antennas Propag.* **1980**, *22*, 191.
(90) Taflove, A.; Hagness, S. C. *Computational Electrodynamics: The Finite-Difference Time-Domain Method*; Artech House Publishers, 2005.
(91) Purcell, E. M.; Pennypacker, C. R. *Astrophys. J.* **1973**, *186*, 705.
(92) Draine, B. T.; Flatau, P. J. *J. Opt. Soc. Am.* **1994**, *11*, 1491.
(93) Kottmann, J. P.; Martin, O. J. F.; Smith, D. R.; Schultz, S. *New J. Phys.* **2000**, *2*, S1367.
(94) Shuford, K. L.; Ratner, M. A.; Schatz, G. C. *J. Chem. Phys.* **2005**, *123*, No. 114713.
(95) Hohenester, U.; Krenn, J. *Phys. Rev. B* **2005**, *72*, No. 195429.
(96) Evlyukhin, A. B.; Bozhevolnyi, S. I. *Phys. Rev. B* **2005**, *71*, No. 134304.
(97) Aizpurua, J.; Bryant, G.; Richter, L.; García de Abajo, F. J.; Kelley, B.; Mallouk, T. *Phys. Rev. B* **2005**, *71*, No. 235420.
(98) Giannini, V.; Sánchez-Gil, J. A. *J. Opt. Soc. Am. A* **2007**, *24*, 2822.
(99) Myroshnychenko, V.; Rodríguez-Fernández, J.; Pastoriza-Santos, I.; Funston, A. M.; Novo, C.; Mulvaney, P.; Liz-Marzán, L. M.; García de Abajo, F. J. *Chem. Soc. Rev.* **2008**, *37*, 1793.
(100) Link, S.; Mohamed, M. B.; El-Sayed, M. A. *J. Phys. Chem. B* **1999**, *103*, 3073.
(101) Payne, E. K.; Shuford, K. L.; Park, S.; Schatz, G. C.; Mirkin, C. A. *J. Phys. Chem. B* **2006**, *110*, 2150.
(102) Bryant, G. W.; García de Abajo, F. J.; Aizpurua, J. *Nano Lett.* **2008**, *8*, 631.
(103) Wiley, B. J.; Chen, Y.; McLellan, J. M.; Xiong, Y.; Li, Z.-Y.; Ginger, D.; Xia, Y. *Nano Lett.* **2007**, *7*, 1032.
(104) Novotny, L. *Phys. Rev. Lett.* **2007**, *98*, No. 266802.
(105) Jain, P. K.; Huang, W.; El-Sayed, M. A. *Nano Lett.* **2007**, *7*, 2080.
(106) Prodan, E.; Radloff, C.; Halas, N. J.; Nordlander, P. *Science* **2003**, *302*, 419.
(107) Ghenuche, P.; Cherukulappurath, S.; Taminiau, T. H.; van Hulst, N. F.; Quidant, R. *Phys. Rev. Lett.* **2008**, *101*, No. 116805.
(108) Schnell, M.; García-Etxarri, A.; Huber, A. J.; Crozier, K.; Aizpurua, J.; Hillenbrand, R. *Nat. Photonics* **2009**, *3*, 287.
(109) Large, N.; Abb, M.; Aizpurua, J.; Muskens, O. *Nano Lett.* **2010**, *10*, 1741.
(110) Langhammer, C.; Kasemo, B.; Zoricl, I. *J. Chem. Phys.* **2007**, *126*, 19470.
(111) Nelayah, J.; Kociak, M.; Stepha, O.; García de Abajo, F. J.; Tence, M.; Henrard, L.; Taverna, D.; Pastoriza-Santos, I.; Liz-Marzán, L. M.; Colliex, C. *Nat. Phys.* **2007**, *3*, 348.
(112) Jin, R.; Cao, Y. W.; Mirkin, C. A.; Kelly, K. L.; Schatz, G. C.; Zheng, J. G. *Science* **2001**, *294*, 1901.
(113) Aizpurua, J.; Hanarp, P.; Sutherland, D. S.; Käll, M.; Bryant, G. W.; García de Abajo, F. J. *Phys. Rev. Lett.* **2003**, *90*, No. 057401.
(114) Hao, F.; Nehl, C. L.; Hafner, J. H.; Nordlander, P. *Nano Lett.* **2007**, *7*, 729.
(115) Hao, E.; Schatz, G. C. *J. Chem. Phys.* **2004**, *120*, 357.
(116) Schuck, P. J.; Fromm, D. P.; Sundaramurthy, A.; Kino, G. S.; Moerner, W. E. *Phys. Rev. Lett.* **2005**, *94*, No. 017402.
(117) Giannini, V.; Sánchez-Gil, J. A. *Opt. Lett.* **2008**, *33*, 899.
(118) Zhang, Z.; Weber-Bargioni, A.; Wu, S. W.; Dhuey, S.; Cabrini, S.; Schuck, P. J. *Nano Lett.* **2009**, *9*, 4505.

(119) Rang, M.; Jones, A. C.; Zhou, F.; Li, Z.-Y.; Wiley, B. J.; Xia, Y.; Raschke, M. B. *Nano Lett.* **2008**, *8*, 3357.
(120) Fano, U. *Phys. Rev.* **1961**, *124*, 1866.
(121) Genet, C.; van Exter, M. P.; Woerdman, J. P. *Opt. Commun.* **2003**, *225*, 331.
(122) Luk'yanchuk, B.; Zheludev, N. I.; Maier, S. A.; Halas, N. J.; Nordlander, P.; Giessen, H.; Chong, C. T. *Nat. Mater.* **2010**, *9*, 707.
(123) Verellen, N.; Sonnefraud, Y.; Sobhani, H.; Hao, F.; Moshchalkov, V. V.; Dorpe, P. V.; Nordlander, P. *Nano Lett.* **2009**, *9*, 1663.
(124) Fedotov, V. A.; Rose, M.; Prosvirnin, S. L.; Papasimakis, N.; Zheludev, N. I. *Phys. Rev. Lett.* **2007**, *99*, No. 147401.
(125) Christ, A.; Martin, O. J. F.; Ekinci, Y.; Gippius, N. A.; Tikhodeev, S. G. *Nano Lett.* **2008**, *8*, 2171.
(126) Bachelier, G.; Russier-Antoine, I.; Benichou, E.; Jonin, C.; Del Fatti, N.; Vallée, F.; Brevet, P.-F. *Phys. Rev. Lett.* **2008**, *101*, No. 197401.
(127) Sonnefraud, Y.; Verellen, N.; Sobhani, H.; Vandenbosch, G. A.; Moshchalkov, V. V.; Dorpe, P. V.; Nordlander, P.; Maier, S. A. *ACS Nano* **2010**, *4*, 1664.
(128) Boller, K.-J.; Imamolu, A.; Harris, S. E. *Phys. Rev. Lett.* **1991**, *66*, 2593.
(129) Liu, N.; Langguth, L.; Weiss, T.; Kästel, J.; Fleischhauer, M.; Pfau, T.; Giessen, H. *Nat. Mater.* **2009**, *8*, 758.
(130) Wang, H.; Brandl, D. W.; Nordlander, P.; Halas, N. *Acc. Chem. Res.* **2007**, *40*, 53.
(131) Nordlander, P.; Oubre, C.; Prodan, E.; Li, K.; Stockman, I. *Nano Lett.* **2004**, *4*, 899.
(132) Arfken, G. B.; Weber, H. J. *Mathematical Methods for Physicists*, 5th ed.; Harcourt Academic Press: London, 2001.
(133) Aubry, A.; Lei, D. Y.; Fernández-Domínguez, A. I.; Sonnefraud, Y.; Maier, S. A.; Pendry, J. B. *Nano Lett.* **2010**, *10*, 2574.
(134) Aubry, A.; Lei, D. Y.; Maier, S. A.; Pendry, J. B. *Phys. Rev. B* **2010**, *82*, No. 125430.
(135) Lei, D. Y.; Aubry, A.; Maier, S. A.; Pendry, J. B. *New. J. Phys.* **2010**, *12*, No. 093030.
(136) Aubry, A.; Lei, D. Y.; Maier, S. A.; Pendry, J. B. *Phys. Rev. Lett.* **2010**, *105*, No. 233901.
(137) Fernández-Domínguez, A.I.; Maier, S. A.; Pendry, J. B. *Phys. Rev. Lett.* **2010**, *105*, No. 266807.
(138) Ashcroft, N. W.; Mermin, N. D. *Solid State Physics*; Thomson Learning: London, 1976.
(139) Wood, R. W. *Philos. Mag.* **1902**, *4*, 396.
(140) Rayleigh, L. *Philos. Mag.* **1907**, *14*, 60.
(141) Carron, K. T.; W.; Fluhr, M. M.; Wokaun, A. *J. Opt. Soc. Am. B* **1986**, *3*, 430.
(142) Markel, V. A. *J. Mod. Opt.* **1993**, *40*, 2281.
(143) Zou, S.; Janel, N.; Schatz, G. C. *J. Chem. Phys.* **2004**, *120* 10871.
(144) Hicks, E. M.; Zou, S.; Schatz, G. C.; Spears, K. G.; Duyne, R. P.; Gunnarsson, L.; Rindzevicius, T.; Kasemo, B.; Käll, M. *Nano Lett.* **2005**, *5*, 1065.
(145) Auguié, B.; Barnes, W. L. *Phys. Rev. Lett.* **2008**, *101*, No. 143902.
(146) Kravets, V. G.; Schedin, F.; Grigorenko, A. N. *Phys. Rev. Lett.* **2008**, *101*, No. 087403.
(147) Chu, Y.; Schonbrun, E.; Yang, E.; Crozier, K. B. *Appl. Phys. Lett.* **2008**, *93*, No. 181108.
(148) Vecchi, G.; Giannini, V.; Gómez Rivas, J. *Phys. Rev. Lett.* **2009**, *102*, No. 146807.
(149) Vecchi, G.; Giannini, V.; Gómez Rivas, J. *Phys. Rev. B* **2009**, *80*, No. 201401.
(150) García de Abajo, F. J. *Rev. Mod. Phys.* **2007**, *79*, 1267.
(151) Zou, S.; Schatz, G. C. *J. Chem. Phys.* **2004**, *121*, 12606.
(152) Quinten, M.; Leitner, A.; Krenn, J. R.; Aussenegg, F. R. *Opt. Lett.* **1998**, *23*, 1331.
(153) Krenn, J. R.; Dereux, A.; Weeber, J. C.; Bourillot, E.; Lacroute, Y.; Goudonnet, J. P.; Schider, G.; Gotschy, W.; Leitner, A.; Aussenegg, F. R.; Girard, C. *Phys. Rev. Lett.* **1999**, *82*, 2590.
(154) Maier, S. A.; Kik, P. G.; Atwater, H. A.; Meltzer, S.; Harel, E.; Koel, B. E.; Requicha, A. A. G. *Nat. Mater.* **2003**, *2*, 229.
(155) Giannini, V.; Vecchi, G.; Gómez Rivas, J. *Phys. Rev. Lett.* **2010**, *105*, No. 266801.
(156) Willets, K. A.; Duyne, R. P. V. *Annu. Rev. Phys. Chem.* **2007**, *58*, 267.
(157) Boltasseva, A. *J. Opt. A: Pure Appl. Opt.* **2009**, *11*, 114001.
(158) Pelton, M.; Aizpurua, J.; Bryant, G. *Laser Photonics Rev.* **2008**, *2*, 136.
(159) Zhang, G.; Wang, D.; Mohwald, H. *Nano Lett.* **2007**, *7*, 127.
(160) Skinner, J. L.; Hunter, L. L.; Talin, A. A.; Provine, J.; Horsley, D. A. *IEEE* **2008**, 7.
(161) Jana, N. R.; Gearheart, L.; Murphy, C. J. *J. Phys. Chem. B* **2001**, *105*, 4065.
(162) Wiley, B.; Sun, Y.; Mayers, B.; Xia, Y. *Chem.—Eur. J.* **2005**, *11*, 454.
(163) Washio, I.; Xiong, Y.; Yin, Y.; Xia, Y. *Adv. Mater.* **2006**, *18*, 1745.
(164) Carbo-Argibay, E.; Rodriguez-Gonzalez, B.; Pacifico, J.; Pastoriza-Santos, I.; Perez-Juste, J.; Liz-Marzan, L. M. *Angew. Chem., Int. Ed.* **2007**, *46*, 8983.
(165) Long, N. N.; Vu, L. V.; Kiem, C. D.; Doanh, S. C.; Nguyet, C. T.; Hang, P. T.; Thien, N. D.; Quynh, L. M. *J. Phys.: Conf. Ser.* **2009**, *187*, No. 012026.
(166) Belloni, J.; Mostafavi, M.; Remita, H.; Marignier, J.-L.; Delcourt, M.-O. *New J. Chem.* **1998**, 1239.
(167) Hund, J. F.; Bertino, M. F.; Zhang, G.; Sotiriou-Leventis, C.; Leventis, N.; Tokuhiro, A. T.; Farmer, J. *J. Phys. Chem. B* **2003**, *107*, 465.
(168) Sonnichsen, C.; Geier, S.; Hecker, N. E.; von Plessen, G.; Feldmann, J.; Ditlbacher, H.; Lamprecht, B.; Krenn, J. R.; Aussenegg, F. R.; Chan, V. Z.-H.; Spatz, J. P.; Moller, M. *Appl. Phys. Lett.* **2000**, *77*, 2949.
(169) Polisski, S.; Goller, B.; Lapkin, A.; Fairclough, S.; Kovalev, D. *Phys. Status Solidi* **2008**, *2*, 132.
(170) Fink, J.; Kiely, C. J.; Bethell, D.; Schiffrin, D. J. *Chem. Mater.* **1998**, *10*, 922.
(171) Mirkin, C. A.; Letsinger, R. L.; Music, R. C.; Storhoff, J. J. *Nature* **1996**, *382*, 607.
(172) Elghanian, R.; Storhoff, J. J.; Mucic, R. C.; Letsinger, R. L.; Mirkin, C. A. *Science* **1997**, *277*, 1078.
(173) Loweth, C. J.; Caldwell, W. B.; Peng, X.; Alivisatos, A. P.; Schultz, P. G. *Angew. Chem., Int. Ed.* **1999**, *38*, 12.
(174) Storhoff, J. J.; Lazarides, A. A.; Mucic, R. C.; Mirkin, C. A.; Letsinger, R. L.; Schatz, G. C. *J. Am. Chem. Soc.* **2000**, *122*, 4640.
(175) Sonnichsen, C.; Reinhard, B. M.; Liphardt, J.; Alivisatos, A. P. *Nat. Biotechnol.* **2005**, *23*, 741.
(176) Wang, H.; Reinhard, B. M. *J. Phys. Chem. C* **2009**, *113*, 11215.
(177) Mastroianni, A. J.; Claridge, S. A.; Alivisatos, A. P. *J. Am. Chem. Soc.* **2009**, *131*, 8455.
(178) Mitchell, C. E. J.; Howard, A.; Carney, M.; Egdell, R. *Surf. Sci.* **2001**, *490*, 196.
(179) Yang, K. Y.; Choi, K. C.; Won, C. *Appl. Phys. Lett.* **2009**, *94*, No. 173301.
(180) Yang, S.-M.; Jang, S. G.; Choi, D.-G.; Kim, S.; Yu, H. K. *Small* **2006**, *2*, 458.
(181) Boltasseva, A.; Nikolajsen, T.; Leosson, K.; Kjaer, K.; Larsen, M. S.; Bozhevolnyi, S. I. *J. Lightwave Technol.* **23**, *1*, 413.
(182) Mailly, D. *Eur. Phys. J.* **2009**, *172*, 333.
(183) Muskens, O. L.; Giannini, V.; Sánchez-Gil, J. A.; Gómez Rivas, J. *Nano Lett.* **2007**, *7*, 2871.
(184) Zhao, X.-M.; Xia, Y.; Whitesides, G. M. *J. Mater. Chem.* **1997**, *7*, 1069.
(185) Vogelgesang, R.; Dmitriev, A. *Analyst* **2010**, *135*, 1175.
(186) Keilmann, F.; Hillenbrand, R. *Philos. Trans. R. Soc. London, Ser. A* **2004**, *362*, 787.
(187) Douillard, L.; Charra, F.; Korczak, Z.; Bachelot, R.; Kostcheev, S.; Lerondel, G.; Adam, P.-M.; Royer, P. *Nano Lett.* **2008**, *8*, 935.
(188) Vesseur, E. J. R.; de Waele, R.; Kuttge, M.; Polman, A. *Nano Lett.* **2007**, *7*, 2843.
(189) Nelayah, J.; Kociak, M.; Stéphan, O.; Geuquet, N.; Henrard, L.; García de Abajo, F. J.; Pastoriza-Santos, I.; Liz-Marzán, L. M.; Colliex, C. *Nano Lett.* **2010**, *10*, 902.

(190) Underwood, S.; Mulvaney, P. *Langmuir* **1994**, *10*, 3427.
(191) Hund, J.; Bertino, M.; Zhang, G.; Sotiriou-Leventis, C.; Leventis, N. *J. Non-Cryst. Solids* **2004**, *350*, 9.
(192) Polisski, S.; Goller, B.; Heck, S. C.; Maier, S. A.; Fujii, M.; Kovalev, D. *Appl. Phys. Lett.* **2011**, *98*, No. 011912.
(193) Sherry, L. J.; Jin, R.; Mirkin, C. A.; Schatz, G. C.; Duyne, R. P. V. *Nano Lett.* **2006**, *6*, 2060.
(194) Yang, S.-C.; Kobori, H.; He, C.-L.; Lin, M.-H.; Chen, H.-Y.; Li, C.; Kanehara, M.; Teranishi, T.; Gwo, S. *Nano Lett.* **2010**, *10*, 632.
(195) Verhagen, E.; Kuipers, L.; Polman, A. *Nano Lett* **2007**, *7*, 334.
(196) Verhagen, E.; Kuipers, L.; Polman, A. *Opt. Express* **2009**, *17*, 14586.
(197) Bouhelier, A.; Bachelot, R.; Lerondel, G.; Kostcheev, S.; Royer, P.; Wiederrecht, G. P. *Phys. Rev. Lett.* **2005**, *95*, No. 267405.
(198) Ash, E. A.; Nicholls, G. *Nature* **1972**, *237*, 510.
(199) Hecht, B.; Sick, B.; Wild, U. P.; Deckert, V; Zenobi, R.; Martin, O. J. F.; Pohl, D. W. *J. Chem. Phys.* **2000**, *112*, 7761.
(200) Mikhailovsky, A. A.; Petruska, M. A.; Stockman, M. I.; Klimov, V. I. *Opt. Lett.* **2003**, *28*, 1686.
(201) Bouhelier, A.; Ignatovich, F.; Bruyant, A.; Huang, C.; des Francs, G. C.; Weeber, J.-C.; Dereux; Wiederrecht, G. P.; Novotny, L. *Opt. Lett.* **2007**, *32*, 2535.
(202) Breit, M.; Malkmus, S.; Feldmann, J.; Danzebrink, H. U. *Appl. Phys. Lett.* **2007**, *90*, No. 093114.
(203) Chu, J.-Y.; Wang, T.-J.; Changa, Y.-C.; Lina, M.-W.; Yeha, J.-T.; Wangb, J.-K. *Ultramicroscopy* **2008**, *108*, 314.
(204) García-Etxarri, A.; Romero, I.; García de Abajo, F. J.; Hillenbrand, R.; Aizpurua, J. *Phys. Rev. B* **2009**, *79*, No. 125439.
(205) Dorfmuller, J.; Vogelgesang, R.; Weitz, R. T.; Rockstuhl, C.; Etrich, C.; Pertsch, T.; Lederer, F.; Kern, K. *Nano Lett.* **2009**, *9*, 2372.
(206) Schnell, M.; Garcia-Etxarri, A.; Huber, A. J.; Crozier, K. B.; Borisov, A.; Aizpurua, J.; Hillenbrand, R. *J. Phys. Chem. C* **2010**, *114*, 7341.
(207) Hillenbrand, R.; Keilmann, F.; Hanarp, P.; Sutherland, D. S.; Aizpurua, J. *Appl. Phys. Lett.* **2003**, *83*, 368.
(208) Taminiau, T. H.; Moerland, R. J.; Segerink, F. B.; Kuipers, L.; van Hulst, N. F. *Nano Lett.* **2007**, *7*, 28.
(209) Betzig, E. B.; Trautman, J. K. *Science* **1992**, *257*, 189.
(210) Vogelgesang, R.; Dorfmüller, J.; Esteban, R.; Weitz, R. T.; Dmitriev, A.; Kern, K. *Phys. Status Solidi (b)* **2008**, *245*, 2255.
(211) Moerland, R. J.; Taminiau, T. H.; Novotny, L.; van Hulst, N. F.; Kuipers, L. *Nano Lett.* **2008**, *8*, 606.
(212) Choi, S.; Park, D.; Lienau, C.; Jeong, M. S.; Byeon, C. C.; Ko, D.-K.; Kim, D. S. *Opt. Express* **2008**, *16*, 12076.
(213) Zavelani-Rossi, M.; Celebrano, M.; Biagioni, P.; Polli, D.; Finazzi, M.; Duó, L.; Cerullo, G.; Labardi, M.; Allegrini, M.; Grand, J.; Adam, P.-M. *Appl. Phys. Lett.* **2008**, *92*, No. 093119.
(214) Nelayah, J.; Gu, L.; Sigle, W.; Koch, C. T.; Pastoriza-Santosa, I.; Liz-Marzn, L. M.; van Aken, P. A. *Opt. Lett.* **2009**, *34*, 1003.
(215) García de Abajo, F. J. *Rev. Mod. Phys* **2010**, *82*, 209.
(216) Schaffer, B.; Werner, G.; Gerald, K.; Ferdinand, H. *Ultramicroscopy* **2010**, *110*, 1087.
(217) Bosman, M.; Keast, V. J.; Watanabe, M.; Maaroof, A. I.; Cortie, M. B. *Nanotechnology* **2008**, *18*, No. 165505.
(218) Ngom, M.; Ringnalda, J.; Mansfield, J. F.; Kotov, N.; Agrawal, A.; Zaluzec, N.; Norris, T. B. Conference on Quantum Electronics and Laser Science; CLEO/QELS, 2008.
(219) Chu, M.-W.; Sharma, P.; Chang, C.-P.; Liou, S. C.; Tsai, K.-T.; Juen-KaiWang; Yuh-LinWang; Chen, C. H. *Nanotechnology* **2009**, *20*, No. 235705.
(220) Koh, A. L.; Bao, K.; Khan, I.; Smith, W. E.; Kothleitner, G.; Nordlander, P.; Maier, S. A.; McComb, D. W. *ACS Nano* **2010**, *3*, 3015.
(221) García de Abajo, F. J.; Kociak, M. *Phys. Rev. Lett.* **2008**, *100*, No. 106804.
(222) Hohenester, U.; Ditlbacher, H.; Krenn, J. R. *Phys. Rev. Lett.* **2009**, *103*, No. 106801.
(223) Douillard, L.; Charra, F.; Fiorini, C.; Adam, P. M.; Bachelot, R.; Kostcheev, S.; Lerondel, G.; de la Chapelle, M. L.; Royer, P. *J. Appl. Phys.* **2007**, *101*, No. 083518.
(224) Bayer, D.; Wiemann, C; Gaier, O.; Bauer, M.; Aeschlimann, M. *J. Nanomater.* **2008**No. 249514.
(225) Kubo, A.; Jung, Y. S.; Kim, H. K.; Petek, H. *J. Phys. B: At. Mol. Opt. Phys.* **2007**, *40*, S259.
(226) Barwick, B.; Flannigan, D. J.; Zewail, A. H. *Nature* **2009**, *462*, 902.
(227) Yamamoto, N.; Araya, K.; García de Abajo, F. J. *Phys. Rev. B* **2001**, *64*, No. 205419.
(228) Gomez-Medina, R.; Yamamoto, N.; Nakano, M.; García de Abajo, F. J., F. J. G. *New. J. Phys.* **2008**, *10*, No. 105009.
(229) Loudon, R. *The Quantum Theory of Light*; Oxford Science Publications: Clarendon, Oxford, U.K., 1973.
(230) Cohen-Tannoudji, F. L. C., Diu, B., Laloe, F. *Quantum Mechanics*; Wiley-VCH: Berlin, 1977.
(231) Purcell, E. M. *Phys. Rev.* **1946**, *69*, 681.
(232) Kuhn, H. *J. Chem. Phys.* **1969**, *53*, 101.
(233) Yeung, M. S.; Gustafson, T. K. *Phys. Rev. A* **1996**, *54*, 5227.
(234) Hankel, C.; Sandoghdar, V. *Opt. Commun.* **1998**, *158*, 250.
(235) Chance, R. R.; Prock, A.; Silbey, R. *Adv. Chem. Phys.* **1978**, *37*, 1.
(236) Ford, G. W.; Weber, W. H. *Phys. Rep.* **1984**, *113*, 195.
(237) Berman, P. R. *Cavity Quantum Electrodynamics*; Academic Press, San Diego, CA, 1994.
(238) Vahala, K. J. *Nature* **2003**, *424*, 839.
(239) Giannini, V.; Sánchez-Gil, J. A.; Muskens, O. L.; Gómez Rivas, J. *J. Opt. Soc. Am. B* **2009**, *26*, 1569.
(240) Taminiau, T. H.; Stefani, F. D.; Segerink, F. B.; van Hulst, N. F. *Nat. Photonics* **2008**, *2*, 234.
(241) Hofmann, H. F.; Kosako, T.; Kadoya, Y. *New J. Phys.* **2007**, *9*, 217.
(242) Li, J.; Salandrino, A.; Engheta, N. *Phys. Rev. B* **2007**, *76*, No. 245403.
(243) Taminiau, T. H.; Stefani, F. D.; van Hulst, N. F. *Opt. Express* **2008**, *16*, 10858.
(244) Curto, A. G.; Volpe, G.; Taminiau, T. H.; Kreuzer, M. P.; Quidant, R.; van Hulst, N. F. *Science* **2010**, *239*, 930.
(245) Chang, D.; Sørensen, A.; Hemmer, P.; Lukin, M. *Phys. Rev. B* **2007**, *76*, No. 35420.
(246) Chang, D. E.; Sørensen, A. S.; Demler, E. A.; Lukin, M. D. *Nat. Phys.* **2007**, *3*, 807.
(247) Chen, Y.; Nielsen, T. R.; Gregersen, N.; Lodahl, P.; Mørk, J. *Phys. Rev. B* **2010**, *81*, 125431.
(248) Giannini, V.; Sánchez-Gil, J.; García-Ramos, J.; Méndez, E. *Phys. Rev. B* **2007**, *75*, No. 235447.
(249) Pellegrini, G.; Mattei, G.; Mazzoldi, P. *Nanotechnology* **2009**, *20*, No. 065201.
(250) Giannini, V.; Sánchez-Gil, J. a.; García-Ramos, J. V.; Méndez, E. R. *J. Chem. Phys.* **2007**, *127*, No. 044702.
(251) Guerrini, L.; García-Ramos, J. V.; Domingo, C.; Sanchez-Cortes, S. *Anal. Chem.* **2009**, *81*, 1418.
(252) Guerrini, L.; Izquierdo-Lorenzo, I.; Rodriguez-Oliveros, R.; Sánchez-Gil, J. A.; Sanchez-Cortes, S.; García-Ramos, J. V.; Domingo, C. *Plasmonics* **2010**, *5*, 273.
(253) Pillai, S.; Catchpole, K. R.; Trupke, T.; Green, M. A. *J. Appl. Phys.* **2007**, *101*, No. 093105.
(254) Lim, S. H.; Mar, W.; Matheu, P.; Derkacs, D.; Yu, E. T. *J. Appl. Phys.* **2007**, *101*, No. 104309.
(255) Catchpole, K. R.; Polman, A. *Opt. Express* **2008**, *16*, 21793.
(256) Ferry, V. E.; Sweatlock, L. A.; Pacifici, D.; Atwater, H. A. *Nano Lett.* **2008**, *8*, 4391.
(257) Haug, F.-J.; Söderström, T.; Cubero, O.; Terrazzoni-Daudrix, V.; Ballif, C. *J. Appl. Phys.* **2008**, *104*, No. 064509.
(258) Rockstuhl, C.; Fahr, S.; Lederer, F. *J. Appl. Phys.* **2008**, *104*, No. 123102.
(259) Rockstuhl, C.; Lederer, F. *Appl. Phys. Lett.* **2009**, *94*, No. 213102.
(260) Kelzenberg, M. D.; Boettcher, S. W.; Petykiewicz, J. A.; Turner-Evans, D. B.; Putnam, M. C.; Warren, E. L.; Spurgeon, J. M.; Briggs, R. M.; Lewis, N. S.; Atwater, H. A. *Nat. Mater.* **2010**, *9*, 239.
(261) Wang, W.; Wu, S.; Reinhardt, K.; Lu, Y.; Chen, S. *Nano Lett.* **2010**, *10*, 2012.

(262) Zhang, W.; Huang, L.; Santschi, C.; Martin, O. J. F. *Nano Lett.* **2010**, *10*, 1006.
(263) Aroca, R. *Surface-Enhanced Vibrational Spectroscopy*; Wiley: Chichester, 2006.
(264) Moskovits, M. *Rev. Mod. Phys.* **1985**, *57*, 783.
(265) Ru, E. C. L.; Etchegoin, P. G. *Principles of Surface-Enhanced Raman Spectroscopy and Related Plasmonic Effects*; Elsevier: Amsterdam, 2009.
(266) Aroca, R. *Surface-Enhanced Vibrational Spectroscopy*; John Wiley: New York, 2006.
(267) Li, J. F.; Huang, Y. F.; Ding, Y.; Li, S. B.; Yang, Z. L.; Zhou, X. S.; Fan, F. R.; Zhang, W.; Zhou, Z. Y.; Wu, D. Y.; Ren, B.; Wang, Z. L.; Tian, Z. Q. *Nature* **2010**, *464*, 392.
(268) Sujith, A.; Itoh, T.; Abe, H.; Anas, A. A.; Yoshida, K.; Biju, V.; Ishikawa, M. *Appl. Phys. Lett.* **2008**, *92*, No. 103901.
(269) Ward, D. R.; Grady, N. K.; Levin, C. S.; Halas, N. J.; Wu, Y.; Nordlander, P.; Natelson, D. *Nano Lett.* **2007**, *7*, 1396.
(270) Stuart, H. R.; Hall, D. G. *Appl. Phys. Lett.* **1998**, *73*, 3815.
(271) Derkacs, D.; Chen, W. V.; Matheu, P. M.; Lim, S. H.; Yu, P. K. L.; Yu, E. T. *Appl. Phys. Lett.* **2008**, *93*, No. 091107.
(272) Matheu, P.; Lim, S. H.; Derkacs, D.; McPheeters, C.; Yu, E. T. *Appl. Phys. Lett.* **2008**, *93*, No. 113108.
(273) Nakayama, K.; Tanabe, K.; Atwater, H. A. *Appl. Phys. Lett.* **2008**, *93*, No. 121904.
(274) Rand, B. P.; Peumans, P.; Forrest, S. R. *J. Phys., Lett.* **2004**, *96*, 7519.
(275) Morfa, A. J.; Rowlen, K. L.; Reilly, T. H.; Romero, M. J.; v. d. Lagemaatb, J. *Appl. Phys. Lett.* **2008**, *92*, No. 013504.
(276) Yablonovitch, E. *J. Opt. Soc. Am.* **1982**, *72*, 899.
(277) Saeta, P. N.; Ferry, V. E.; Pacifici, D.; Munday, J. N.; Atwater, H. A. *Opt. Express* **2009**, *17*, 20975.
(278) Yu, Z.; Raman, A.; Fan, S. *Proc. Natl. Acad. Sci. U.S.A.* **2009**, *107*, 17491.
(279) Faulk, W. P.; Taylor, G. *Immunochemistry* **1971**, *8*, 1081.
(280) Yang, D.-P.; Cui, D.-X. *Chem.—Asian J.* **2008**, *3*, 2010–2022.
(281) Lee, S.; Cha, E.-J.; Park, K.; Lee, S.-Y.; Hong, J.-K.; Sun, I.-C.; Kim, S. Y.; Choi, K.; Kwon, I. C.; Kim, K.; Ahn, C.-H. *Angew. Chem., Int. Ed.* **2008**, *47*, 2804.
(282) Boisselier, E.; Astruc, D. *Chem. Soc. Rev.* **2009**, *38*, 1759.
(283) Debouttière, P.-J.; Roux, S.; Vocanson, F.; Billotey, C.; Beuf, O.; Favre-Réguillon, A.; Lin, Y.; Pellet-Rostaing, S.; Lamartine, R.; Perriat, P.; Tillement, O. *Adv. Funct. Mater.* **2006**, *16*, 2330.
(284) Liu, X.; Lloyd, M. C.; Fedorenko, I. V.; Bapat, P.; Zhuokov, T.; Huo, Q. *Nanomedicine* **2008**, *5*, 617.
(285) Hleb, E. Y.; Hafner, J. H.; Myers, J. N.; Hanna, E. Y.; Rostro, B. C.; Zhdanok, S. A.; Lapotko, D. O. *Nanomedicine* **2008**, *5*, 647.
(286) Govorov, A. O.; Zhang, W.; Skeini, T.; Richardson, H.; Lee, J.; Kotov, N. A. *Nanoscale Res. Lett.* **2006**, *1*, 84.
(287) Govorov, A. O.; Richardson, H. *Nanotoday* **2007**, *2*, 30.
(288) Baffou, G.; Quidant, R.; Girard, C. *Appl. Phys. Lett.* **2009**, *94*, No. 153109.
(289) Baffou, G.; Girard, C.; Quidant, R. *Phys. Rev. Lett.* **2010**, *104*, No. 136805.
(290) Baffou, G.; Quidant, R.; Girard, C. *Phys. Rev. B* **2010**, *82*, No. 165424.

## NOTE ADDED AFTER ASAP PUBLICATION

This paper was published to the Web on 3/24/2011, with an error in figure 6. The correct version was published to the Web on 5/10/2011.